Aerosols-precipitation elevation dependence over the Central Himalayas using cloud-resolving WRF-Chem numerical modeling

Pramod Adhikari[1, 2] John F. Mejia[1, 2]

[1] *Division of Atmospheric Sciences, Desert Research Institute, Reno, Nevada, USA*

[2] *Atmospheric Sciences Graduate Program, University of Nevada, Reno, Nevada, USA*

Correspondence to: Pramod Adhikari (adhik.pramod@nevada.unr.edu) and John F. Mejia (john.mejia@dri.edu)

12   **Abstract**

13   Atmospheric aerosols can modulate the orographic precipitation impacting the evolution of clouds through radiation

14   and microphysical pathways. This study implements the cloud-resolving Weather Research and Forecasting model

15   coupled with chemistry (WRF-Chem) to study the response of the Central Himalayan elevation-dependent

16   precipitation to the atmospheric aerosols. The first monsoonal month of 2013 is simulated to assess the effect of

17   aerosols through radiation and cloud interactions. The results show that the response of diurnal variation and

18   precipitation intensities (light, moderate, and heavy) to aerosol radiation and cloud interaction depended on the

19   different elevational ranges of the Central Himalayan region. Below 2000 m ASL, the total effect of aerosols

20   resulted in suppressed mean light precipitation by 19% while enhancing the moderate and heavy precipitation by 3%

21   and 12%, respectively. In contrast, above 2000 m ASL, a significant reduction of all three categories of precipitation

22   intensity occurred with the 11% reduction in mean precipitation. These contrasting altitudinal precipitation

23   responses to the increased anthropogenic aerosols can significantly impact the hydroclimate of the Central

24   Himalayas, increasing the risk for extreme events and influencing the regional supply of water resources.

1. Introduction

The south Asian summer monsoon system, one of the major monsoonal systems on Earth, is located in the region with the persistent occurrence of substantial loadings of atmospheric aerosols (Li et al., 2016). The densely populated and rapidly growing urban centers of the Indo-Gangetic Plain (IGP), located over northern India at the foothills of the Himalayas, experience frequent events of severe air pollution with significant contribution from local anthropogenic activities and remotely transported mineral dust aerosols (Dey and Di Girolamo, 2011; Kumar et al., 2018; Sijikumar et al., 2016). Atmospheric aerosols, from both natural and anthropogenic sources, can impact the weather and climate on a local to global scale through interactions with radiation and cloud, as well as through albedo and hydrologic pathways due to deposition over the snow (e.g., Sarangi et al., 2019; Wu et al., 2018; Andreae and Rosenfeld, 2008; Haywood and Boucher, 2000; Mahowald et al., 2011; Ramanathan and Carmichael, 2008). However, due to inhomogeneous distribution and complex radiation and cloud interaction, aerosol also contributes to the larger uncertainties in assessing the Earth's changing climate (IPCC, 2013).

The Aerosol-Radiation Interaction (ARI) comprises the direct radiative effects, which include the scattering and absorption of solar radiation depending on the optical properties, and the semi-direct effect (IPCC, 2013). The semi-direct effect refers to the heating of the cloud due to the absorbing aerosols, which reduces the relative humidity and increases the cloud burn-off process resulting in lower planetary albedo (Hansen et al., 1997; Huang et al., 2006a; Ackerman et al., 2000). The ARI can alter the surface energy budget, atmospheric thermodynamic structure, convective stability, and tropical-meridional circulation, in turn modulating the frequency and intensity of the monsoonal rainfall (e.g., Li et al., 2016; Ramanathan et al., 2005; Lau et al., 2006). At a daily timescale, due to the direct radiative effect increases the low-level stability over the polluted urban plains resulting in enhanced moisture transport towards the downwind mountains and abnormally increasing precipitation (Choudhury et al., 2020; Fan et al., 2015).

IPCC (2013) refers to the Aerosol-Cloud Interaction (ACI) to the modification of cloud microphysical properties or cloud evolution through the ability of aerosol to act as cloud condensation nuclei (CCN) or Ice-Nucleating particles (INPs). Polluted clouds or clouds with a higher concentration of CCN increase the number of smaller cloud droplets for a constant liquid water path and enhances the reflection, also known as the first indirect effect (Twomey, 1977). Smaller cloud droplets result in increased cloud lifetime and height and suppress the drizzle precipitation, also known as the second indirect or cloud lifetime effect (Pincus and Baker, 1994; Albrecht, 1989; Rosenfeld, 1999). The continuing and intensified updrafts with the release of latent heat of condensation and freezing and additional thermal buoyancy invigorate the convection strength and cloud development (Rosenfeld et al., 2008; Andreae et al., 2004; Koren et al., 2005). Additionally, Fan et al. (2017) proposed that the increase in latent heat release with CCN concentration strengthens the moisture transport to the windward slope and can invigorate the mixed phase orographic clouds resulting in higher precipitation over the Sierra Nevada, California.

The locally emitted and transported anthropogenic aerosols can impact the precipitation, vertical temperature distribution, and regional hydroclimate of the Himalayan and the adjacent region. The deep convective activity and southwesterly monsoonal flow incorporate the remote dust and anthropogenic aerosols from the IGP

62 and transports them to the southern slopes of the Himalayas and even to the Tibetan Plateau (Kang et al., 2019; Ji et
63 al., 2015; Vernier et al., 2011). Adhikari and Mejia (2021) indicated that the heavier aerosol loadings contribute to
64 the increased freezing isotherm over the Central Himalayas during the monsoonal season. The increasing trend of
65 the freezing level height (FLH) has been reported around the globe (e.g., Wang et al., 2014; Bradley et al., 2009;
66 Zhang and Guo, 2011; Prein and Heymsfield, 2020; Lynn et al., 2020), and can impact the snowline altitude (Wang
67 et al., 2014; Prein and Heymsfield, 2020). The amplified warming of the mountainous terrain or the elevation-
68 dependent warming around the globe can also be associated with the change in snow cover and albedo, radiative and
69 surface fluxes, changes in water vapor and latent heat release, deposition of aerosols on snowpack, and aerosol
70 concentrations (Pepin et al., 2015; Rangwala et al., 2010). Depending on the location and topographical altitude,
71 different factors can dominate elevation-dependent warming; e.g., the radiative impact of concentrated aerosol
72 loading can play a significant role in modulating the temperature over the slopes of the Himalayas and mid-latitude
73 Asia (Pepin et al., 2015; Rangwala and Miller, 2012; Palazzi et al., 2017).

74 The atmospheric heating due to the accumulated remote dust and carbonaceous aerosols from IGP leads to
75 the northward shift of deep convection and heavier monsoonal rainfall over the foothills of the Himalayas during the
76 early monsoon period (Lau et al., 2006, 2017). Furthermore, the variability in the orographic precipitation has also
77 been linked to the atmospheric aerosols around the globe (Napoli et al., 2019; Wu et al., 2018; Choudhury et al.,
78 2020; Adhikari and Mejia, 2021, 2022). Barman and Gokhale (2022), using a coarse (10 km) resolution WRF-Chem
79 simulation, showed aerosol could modulate the precipitation over the mountainous terrain of north-eastern India
80 during the spring season. Also, a case study by Adhikari and Mejia (2022) showed Central Himalayan early
81 monsoon precipitation enhanced due to the remotely transported dust aerosols. Cho et al. (2016) suggested that
82 anthropogenic climate forcing modifies the circulation structure, triggers the intense rainfall over northern south
83 Asia, and increases the risk of flood severity. Furthermore, long term observational studies by Choudhury et al.
84 (2020) and Adhikari and Mejia (2021) showed that the aerosol invigorated cloud development and enhanced the
85 precipitation over the southern slopes of the central Himalayas. The localized extreme weather events over the
86 complex mountainous terrain pose a higher hazard due to flash floods and landslides.

87 The increased aerosols over the slopes of the Himalayas impacts the microphysical properties of the clouds and
88 can modulate the precipitation pattern over the different elevational band of the Himalayas (Palazzi et al., 2013;
89 Dimri et al., 2022). The climatology of the temperature and precipitation trends and elevational dependence over the
90 Tibetan Plateau (TP) and the Himalayas was recently studied using the climate models (e.g., Palazzi et al., 2017;
91 Ghimire et al., 2018; Dimri et al., 2022), but without including the effect of aerosols. To the best of our knowledge,
92 a study examining the elevation dependence of aerosol-cloud interaction and precipitation response to aerosols over
93 the Central Himalayan region is lacking. A better understanding of aerosol-cloud interaction on elevation-dependent
94 precipitation and temperature of this mountainous region is crucial to assess the hydrologic and climate risks for
95 millions of people residing on the adjacent lowlands. This study seeks to examine whether there is an asymmetrical
96 aerosol-cloud response in the orographic forcing process over the southern slopes of the Himalayas and further
97 estimate and evaluate the role of increased anthropogenic aerosols in modulating the surface temperature
98 distribution along the elevational band. To achieve this goal, we implement the Weather Research and Forecasting

99 (WRF) model coupled with chemistry (WRF-Chem) configured at a cloud-resolving scale (3 km), where the

100 organization of the convection is explicitly resolved, for the first monsoonal month of 2013 after the onset of the

101 monsoon in Nepal. To understand the processes involved in the aerosol-cloud interaction and precipitation-elevation

102 dependence, WRF-Chem simulation realizations were performed to isolate the contribution of the ACI and ARI. In

103 section 2, we describe the details of the model used. In section 3, we present and discuss the model evaluation and

104 simulation results. The conclusion of this study is summarized in section 4.

2. Methodology

2.1 Model description

107 In this study, we implement the Weather Research and Forecasting (WRF) model coupled with Chemistry

108 (WRF-Chem) version 4.1.5 for numerical simulations (Grell et al., 2005). WRF-Chem is an advanced online

109 coupled regional model which can simulate the emission, transport, and transformation of trace gases and aerosols

110 with atmospheric feedback processes from radiation and meteorology (Chapman et al., 2009; Fast et al., 2006).

111 WRF-Chem consists of several chemistry components, e.g., emission inventories, aerosol-chemistry mechanism,

112 aqueous and gas phase mechanism, dry and wet deposition, and photolysis, and has been widely used to study

113 aerosol emission and transport (e.g., Dhital et al., 2022; Parajuli et al., 2019) and aerosol-cloud-radiation-climate

114 interaction (e.g., Wu et al., 2018; Fan et al., 2015; Sarangi et al., 2015; Archer-Nicholls et al., 2016; Liu et al., 2020)

115 around the globe.

116 The Carbon Bond Mechanism (CBM-Z; Zaveri and Peters 1999), a gas-phase chemistry mechanism coupled

117 with the MOSAIC (Model for Simulating Aerosol Interactions and Chemistry; Zaveri et al. 2008) aerosol module,

118 was utilized. The CBM-Z includes 67 chemical species and 164 reactions and treats the organic compound in a

119 lumped structure approach depending on their internal bond types (Gery et al., 1989; Zaveri et al., 2008). MOSAIC

120 aerosol module simulates all the major aerosol species (including sulfate, nitrate, ammonium, primary organic mass,

121 black carbon, and liquid water) that are deemed to be significant at urban, regional, and global scales (Zaveri et al.,

122 2008). Of note is that the MOSAIC version implemented in this study does not treat the secondary organic aerosols,

123 which are expected to modulate the physical and chemical properties of atmospheric aerosols (Kaul et al., 2011;

124 Hallquist et al., 2009) and can add up the uncertainties in the result. The aerosol size distribution within the

125 MOSAIC aerosol module is represented by a 4 or 8 sectional bin approach. To reduce the computational burden, the

126 aerosol size distribution in the MOSAIC was represented using 4-bins, ranging between 39 nm to 10 µm based on

127 dry particle diameters. The four bin approach reasonably produces similar results in comparison to the eight sized

128 bins approach (Eidhammer et al., 2014; Zhao et al., 2013). All particles within a bin are considered to be internally

129 mixed, which have similar chemical composition, while particles from different sized bins are mixed externally

130 (Zaveri et al., 2008).

131 Composite aerosol optical properties, such as the extinction and scattering coefficient, single scattering albedo,

132 and asymmetry factor, are estimated as a function of the size and chemical composition of aerosols using the volume

133 averaging method with Mie theory (Fast et al., 2006; Chapman et al., 2009). The total integrated aerosol optical

134 properties across all sized bins are then used in the radiation transfer scheme to compute the net radiative effect of

135 aerosols (Chapman et al., 2009; Iacono et al., 2008). The primary aspect of aerosols in impacting cloud evolution

136 and microphysics are the concentration and composition, size distribution, and hygroscopic nature of aerosols

137 (Khain et al., 2016). In a convective cloud, the effect of aerosols on the microphysics is mainly determined by the

138 number of aerosols activated as CCN, which impacts the size and cloud droplet number concentration (Chapman et

139 al., 2009). Aerosols are activated as CCN when the maximum environmental supersaturation is greater than the

140 critical supersaturation of an aerosol, which is a function of aerosol size and composition. The maximum

141 supersaturation of rising air parcels within each size bin is computed as a function of vertical velocity and

142 composition of internally mixed aerosols (Abdul-Razzak and Ghan, 2002). The interstitial aerosols with higher

143 critical supersaturation than maximum ambient supersaturation are not activated as CCN (Chapman et al., 2009).

144 Also, the WRF-Chem can resuspend cloud-borne aerosols to an interstitial state when the cloud particles evaporate

145 within a grid cell (Chapman et al., 2009). The main advantage of using cloud-resolving scales in this aerosol-cloud

146 interacting study is that the activation of aerosols is explicitly resolved by the double-moment microphysics scheme

147 (Archer-Nicholls et al., 2016; Chapman et al., 2009; Yang et al., 2011).

148   This study uses the anthropogenic emission inventories from the Emission Database for Global

149 Atmospheric Research-Hemispheric Transport of Air Pollutants (EDGAR-HTAP) and EDGARv4.3.2 (Janssens-

150 Maenhout et al., 2015). EDGAR-HTAP is a global monthly emission inventory for the year 2010 at a spatial

151 resolution of 0.1° × 0.1°. EDGAR-HTAP emission inventory includes the black carbon, organic matter, particulate

152 matter, ammonia, sulfates, oxides of nitrogen, and carbon monoxide, from the major anthropogenic sources from

153 power generation, industry, residential, agriculture, ground and aviation transport, and shipping. The non-methane

154 volatile organic compounds in this study are provided from EDGARv4.3.2. This study utilizes the biogenic

155 emissions from the Model of Emissions of Gases and Aerosols from Nature (MEGAN), which quantifies the net

156 emissions from the terrestrial biosphere at a horizontal resolution of one square km (Guenther et al., 2006, 2012).

157 Fire INventory from NCAR version 1.5 (FINNv1.5), which provides the global estimates of open episodic fires from

158 different sources in a 1 km spatial and daily temporal resolution (Wiedinmyer et al., 2011), is used as biomass

159 burning emissions. Though fire events are less relevant during the monsoon season (2002-2013) in our area of

160 interest (Matin et al., 2017), we used biomass burning information to include all the primary sources of aerosols.

161   The Community Atmosphere Model with Chemistry (CAM-Chem), with 0.9° × 1.25° spatial resolution

162 with 56 vertical levels and six hourly temporal resolution, is used as initial and boundary conditions for the chemical

163 species (Buchholz et al., 2019). The meteorological forcing in CAM-Chem is driven by Modern-Era Retrospective

164 analysis for Research and Applications version 2 (MERRA2) reanalysis product (Emmons et al. 2020). Furthermore,

165 the Coupled Model Intercomparison Project round 6 (CMIP6) provides the anthropogenic aerosols within CAM-

166 Chem. The ERA5 (Hersbach et al., 2020), a most recent reanalysis product from European Centre for Medium range

167 Weather Forecasting (ECMWF), with 31 km spatial and hourly temporal resolution, was used to initialize the model

168 and as boundary conditions for the basic meteorological state parameters.

169 **2.2 Experimental setup**

170   According to the Department of Hydrology and Meteorology (DHM) of Nepal, the onset of the monsoon
171   occurred on June 14th, 2013, about a day after a normal onset date over eastern Nepal (DHM Nepal, 2022), and
172   generally, over the entire country within a week. Model simulations were performed for 31 days, from June 14th 00
173   UTC to July 15th 00 UTC, 2013. The mean precipitation over the Central Himalayan region (hereafter "CenHim";
174   area indicated by the white-colored polygon in Fig. 1b) during the first month of the monsoon (31 days after the
175   monsoonal onset) from 2000-2021 is 11.84 mm/day with a standard deviation of 2.97 mm/day (see Fig. S1). For the
176   same period, the CenHim region in 2013 received 14.62 mm/day of precipitation which is within +1 standard
177   deviation of the climatology mean.

178   Two one-way nested domains with a horizontal resolution of 9 km and 3 km were set up (see Fig. 1). The
179   model was divided into 61 vertical layers with the 50 hPa model top. The 9 km parent domain with 179×221 grids
180   covered the central and northern/eastern India, Bangladesh, Bhutan, and TP. The 3 km nested domain with $273 \times$
181   321 grid points was designed to include the CenHim, Nepal (with Mount Everest), the areas of most anthropogenic
182   emission sources over the central IGP, and the immediate Himalayan plateau region of Tibet. The summary of the
183   model configuration with the physical parameterizations used in this study is listed in Table 1. The model physics
184   scheme used in the simulation included Morrison-double moment for microphysics, Yonsei University (YSU) for
185   the boundary layer, Rapid Radiative Transfer Model for General Circulation Models (RRTMG) for radiation, and
186   Unified Noah for the land surface. The double moment Morrison microphysics scheme simulates the number and
187   mass mixing ratio of hydrometeors, including cloud droplets, rain, ice, snow, and graupel (Morrison et al., 2009).
188   Previous studies have reasonably implemented the Morrison microphysics, RRTMG, and YSU to simulate and study
189   the aerosol-cloud-precipitation interaction on a cloud-resolving scale (e.g., Kant et al., 2021; Wu et al., 2018). Grell-
190   3D cumulus parameterization scheme (Grell and Dévényi, 2002) was used for the outer 9 km domain for the
191   cumulus parameterization, while no parameterization was used for the inner 3 km domain. This consideration
192   assumes that the model explicitly resolves convective eddies for the 3 km domain, hence the term cloud-resolving
193   scale. The convection parameterization is linked to significant sources of uncertainty in larger-scale models (Prein et
194   al., 2015), and it is recommended to use a cloud-resolving scale to assess the indirect effect of aerosols in a
195   convective system (Grell et al., 2011; Archer-Nicholls et al., 2016). Furthermore, such fine resolution is necessary to
196   adequately address the altitudinal gradient in the steep mountains with characteristic altitudes ranging from 60 to
197   8000 m ASL in about 200 km horizontal distance.

198   Three simulations were performed to assess the sensitivity of the model to aerosol effects. A baseline or
199   control simulation (hereafter "CTL") includes all the emissions (anthropogenic, biogenic, fire, and aerosols from
200   chemistry boundary conditions). CTL includes the aerosol-radiation interaction, indirect effect of aerosols, wet
201   scavenging, and dry deposition of aerosols. To isolate the direct effect of aerosol, the second simulation that
202   resembles the CTL simulation is performed, but by turning off aerosol-radiation interaction (hereafter "NoARI").
203   The comparison between the CTL and NoARI enables the assessment of effect of aerosol-radiation interaction (ARI
204   effect; Wu et al., 2018). The third experiment resembles the CTL, but it is performed by multiplying the
205   anthropogenic aerosols from the boundary condition and emission inventory by a factor of 10% (hereafter
206   "CLEAN"). Reducing polluted aerosol concentration to a more pristine environment has been implemented

207 previously in studying the impact of aerosols on clouds and precipitation (e.g., Manoj et al., 2021; Fan et al., 2013,
208 2007). Since the CLEAN scenario is not entirely aerosol-free, the presence of the 10% anthropogenic aerosols and
209 contribution from the fire and biogenic emissions can influence the assessment of the ACI effect. So, we attempt to
210 broadly examine the microphysical effect of anthropogenic aerosols by comparing NoARI to CLEAN simulations
211 (ACI effect). For completeness and as an effort to assess the uncertainty of anthropogenic aerosol loading in the
212 region, a fourth simulation was performed using CTL but doubling aerosol concentration (D_AERO). Early results
213 in this study suggested that the CTL simulation predicted a relatively low AOD compared to remote sensing
214 retrievals. We use results and discuss the effect of the D_AERO simulations when necessary. Also, unless
215 mentioned, we examine and present the results using the analysis from the inner domain.

216   To examine the aerosol-precipitation elevational dependence, we divided the CenHim into 30 different bins
217 at an increasing interval of 200 m up to 6000 m and one bin for elevation above 6000 m above sea level (ASL).
218 Figure 2 shows the elevation distribution of the number of grid points in the CenHim and the corresponding mean
219 CTL precipitation. The relatively small number of grid points at higher elevations suggests a drop in the statistical
220 robustness of the analyses. When possible, we perform statistical significance tests using the student's t-test at the
221 90% confidence level to control for the statistical signal and noise. The maximum number of grid points (7113) is
222 present below 200 meters, while only 176 grid points are present above 6000 meters over the CenHim. The diurnal
223 variation and the elevational dependency of each variable are obtained by computing the average among all the grid
224 points within each bin of the elevational range.

2.3 Model Evaluation

226   CTL precipitation fields were evaluated using the sparsely distributed network of 90 rain gauge stations
227 measuring daily accumulations (measured at 03 UTC) and provided by the Department of Hydrology and
228 Meteorology, Nepal (see Fig. 1b). The altitudinal station distribution ranges from 60 to 2744 m ASL. The spatial
229 distribution of simulated precipitation was compared with the half-hourly Integrated Multi-satellite Retrievals for
230 Global Precipitation Measurement (IMERG) level-3 data at 0.1° × 0.1° horizontal resolution (Huffman et al., 2019).

231   CTL simulated 550 nm Aerosol Optical Depth (AOD) is evaluated against the AOD retrievals from four
232 ground-based Aerosol Robotic Network (AERONET version 3 level 2.0; Kathmandu Bode, Pokhara, Kanpur, and
233 Jaipur; see Fig. 1a), satellite-based Moderate Resolution Imaging Spectroradiometer available at 10 km grid size
234 [MODIS Terra (MOD04_L2; sensed at 1030 LST) and Aqua (MYD04_L2; sensed at 1330 LST)], and MERRA2
235 reanalysis product (three hourly; 0.5° × 0.625° spatial resolution). The spatial distribution of simulated AOD is
236 compared with MODIS (level 3; 1°×1°) and MERRA2 reanalysis product (three hourly; 0.5° × 0.625° spatial
237 resolution). The combined Dark Target and Deep Blue 550 nm AOD product from Terra and Aqua on-board
238 MODIS satellites are used for comparison. AERONET AOD data were obtained for 1000 to 1100 LST (±30 minutes
239 of Terra overpass time) and 1300 to 1400 LST (±30 minutes of Aqua overpass time) to match up the MODIS
240 overpass times. For time consistency, we used 1045 LST (0500 UTC) and 1345 LST (0800 UTC) as the nearest
241 simulated AOD times. The AERONET and MODIS retrievals of aerosol properties are limited during the
242 monsoonal season since they provide the AOD data measured in cloud-free conditions.

243   Since no upper air soundings are available in CenHim, radiosonde observations from the

244   http://weather.uwyo.edu/upperair/sounding.html at the Patna station, located south of CenHim, (25.60°N, 85.1°E, 60

245   m ASL, only available at 00 UTC; see Fig. 1a) was used to evaluate upper-air meteorological parameters

246   (temperature, zonal and meridional wind components, and mixing ratio). Sounding data was interpolated at 36

247   pressure levels between 100 and 975 hPa with an increment of 25 hPa.

3. Results and Discussion

3.1 Model Evaluation

250   Figure 3 shows the time series of the simulated AOD compared with the ground and satellited based AOD from

251   AERONET and MODIS Aqua and Terra. Though limited data points are available for comparison, the CTL

252   consistently underestimated the AOD, while D_AERO is comparable in magnitude with remotely sensed AOD (Fig.

253   3). Figure 4 shows the spatial distribution of mean MODIS, MERRA2, and simulated AOD during the simulation

254   period. Though the CTL underestimated the AOD in magnitude, it captured the spatial distribution of AOD

255   compared to the MODIS (Fig. 4a) and MERRA2 (Fig. 4b). Due to the higher emission rate, the aerosol is heavily

256   concentrated over the foothills and the IGP compared to the higher elevation of the mountainous terrain. The

257   variation in the AOD along with the topographical transect from lower to higher elevation is clearly illustrated in

258   Fig. 4. Not surprisingly, simulated AOD is lower for the CLEAN simulation over the entire domain, with the

259   differences being maximum in the lowlands (Fig. 4b). Although higher mountainous terrain is polluted compared to

260   the CLEAN scenario, the CTL AOD shows that it remains pristine compared to IGP due to the strong stratification

261   of aerosol emission with elevation and limited transport due to the topographical barrier. The doubling of the

262   anthropogenic aerosols in D_AERO resulted in increased AOD comparable to the MODIS and MERRA2 products

263   (Fig. 4d). It should be noted that the MODIS and MERRA2 are at coarser resolution and might have some biases

264   related to the scale differences.

265   Underestimation of AOD by WRF-Chem is a well-known model bias and has also been reported in the east

266   Asian monsoon region (Wu et al., 2013), Indian monsoon region (Soni et al., 2018; Govardhan et al., 2015), and

267   Indo Gangetic Plain during monsoon by around 50% (Sarangi et al., 2015). Also, Regional Climate Model

268   (RegCM4) underestimated AODs by a factor of 2 to 5 over south Asia in the period 2005 to 2007 (Nair et al., 2012).

269   Mues et al. (2018) showed that the EDGAR HTAP v2.2 implemented with WRF-Chem underestimates the black

270   carbon concentration over the Kathmandu valley by 80% in May of 2013, and one of the reasons might be the

271   underrepresentation of mobile emissions. The lower estimation of the aerosol emission over Nepal by the global

272   emission inventory is mainly due to the coarser resolution, emission factors, and lack of residential energy

273   consumption consideration (Sadavarte et al., 2019). Other limitations that might contribute to the lower estimation

274   of aerosol loading might be due to the different year used for emission inventory preparation (for 2010) and

275   simulation in this study, the lack of representation of secondary organic aerosols, and not accounting for all major

276   sources of emissions (e.g., emission due to infrastructure construction). Despite these well-known structural errors

277   that have been attributed to emissions inventory and potentially result in low biases in the impact of aerosols, our

278   results can provide meaningful insight into the role of aerosols in modulating the elevation dependence precipitation.

279   The mean temperature, mixing ratio, and zonal and meridional wind bias profiles from the simulated output
280   sampled from the upper air sounding observations at the Patna location are shown in Fig. S2. The model exhibits the
281   vertical easterly systematic bias between 950 and 300 hPa. Above 900hPa, a dry bias (significant above 575 hPa)
282   and northerly biases are present. The cool bias prevails below 775 hPa, while the warm bias is present in the mid-to-
283   upper troposphere. Though both the domains revealed a similar biases pattern, the cloud-resolving domain exhibited
284   smaller biases.

285   Figure 5 shows the error statistics of daily precipitation at different gauge stations and simulated precipitation at
286   the nearest grid point over Nepal. The biases in the simulated precipitation varied with elevation, where low-land
287   areas (< 500 m ASL) depicted the larger bias, while the altitude between 500 and 1500 m exhibited the smallest
288   bias. The mean bias estimation (MBE) across the rain gauge stations was lower by 0.29 mm/day with a mean root
289   mean square error (RMSE) of 27.52 mm/day. The daily mean accumulated precipitation from the model correlated
290   well (correlation coefficient of 0.5) with the gauge station data. The maximum mean correlation was observed for
291   the elevation between 500 and 1500 meters, the range of altitude that also depicted the minimum RMSE and MAE.
292   Though some over or underestimation of the precipitation and higher RMSE, there is a good agreement between the
293   onset and accumulated precipitation between the simulation and rain gauge stations (Fig. 5e-h). Also, as suggested
294   earlier, the lower concentration of aerosols can add up to the biases in the simulated precipitation. The manual
295   recording of the gauge station data and the under catch or losses due to wind speed/direction can add up to the
296   uncertainties in the precipitation data collection (Talchabhadel et al., 2017) and these model evaluation assessments.
297   Also, since most rain gauge stations are over the valley floor, the precipitation simulated over the mountain top
298   cannot be compared with the observational network.

299   Figure 6 shows the mean hourly precipitation estimates from IMERG, CTL, and the bias of CTL relative to the
300   IMERG estimation. Compared to IMERG, the model underestimated the precipitation amount over the IGP, while
301   the wet bias of the model is pronounced over the mountains of the CenHim. In general, though some biases in
302   precipitation exist, the model showed the overall feature of the precipitation distribution with lower rainfall over the
303   lowlands, maximum mountainous precipitation associated with orographic forcing, and reduced leeward
304   precipitation over northwestern Nepal and the TP. The point precipitation pattern over the peaks of the mountain
305   might be due to the strong orographic lifting associated with the convective cells. The overestimation of the
306   precipitation by the WRF-Chem has also been reported in other studies over the Himalayan region (e.g., Barman and
307   Gokhale, 2022; Sicard et al., 2021; Adhikari and Mejia, 2022) and can be associated with the uncertainties from the
308   physical parameterizations (e.g., Baró et al., 2015; Zhang et al., 2021). However, note that the finer resolution
309   simulation better resolves the orographic forcing and can represent the precipitation over the complex terrain. Also,
310   IMERG is at a coarser resolution than the model, and some biases might be related to the scale differences. The
311   underprediction of accumulated precipitation by IMERG is evident over the rain gauge stations throughout the
312   CenHim (Fig. 5e-h) and is consistent with the (Sharma et al., 2020a). The pronounced differences over the higher
313   terrains of CenHim can also be associated with the underprediction of extreme precipitation events (> 25mm/day) by
314   IMERG (Sharma et al., 2020b), which might be related to the weak detection of shallow orographic forced
315   precipitation event (Cao et al., 2018; Arulraj and Barros, 2019; Shige and Kummerow, 2016).

3.2 Aerosol Effect on Precipitation

Figure 7 (a-c) shows the effect of aerosol on the spatial distribution of the mean hourly precipitation. Due to the total effect of aerosols, precipitation increases over the elevation below 2000 m ASL except for the region just south of Nepal, with a pronounced enhancement by the ACI effect. At the same time, the reduced precipitation occurred over the high elevational region of the entire CenHim due to the total effect of aerosol. Figure 8a shows the diurnal variation of precipitation as a function of terrain elevation. Minimum precipitation occurred throughout the elevations during the late morning (0900 to 1200 local time). The mid-altitude range, especially between 1000 and 2000 m ASL, of CenHim experiences double peaks with stronger daytime and weaker nighttime precipitation (Fig. 8a). The averaging of the entire CenHim might influence the diurnal features of intraregional precipitation; however, the diurnal pattern is consistent with the satellite-based findings of Fujinami et al. (2021). The surface heating and the orographic forcing enhance the convergence of daytime upslope moisture flow resulting in higher daytime precipitation over the southern slopes (Fujinami et al., 2021). In contrast, the adjacent foothills (below 600 m ASL) are characterized by single midnight to early morning peak due to the convergence of stronger nocturnal jets with the downslope winds (Fujinami et al., 2021; Terao et al., 2006). Precipitation over the higher elevation above 5000 m ASL and in the TP (not shown) is characterized by the afternoon peak and is consistent with Liu et al. (2022).

The diurnal variation of precipitation due to the aerosols effect as a function of elevation is presented in Fig. 8 (b-d) and shows an inconsistent response to the anthropogenic aerosols along the elevational gradient. Significant enhancement of precipitation occurred due to aerosols over the lower elevation (below 2000 m ASL) from the early morning to noon. In contrast, the aerosol suppressed afternoon (1400 to1800 local time) precipitation over the lower elevation. The significant suppression of precipitation is observed over the higher terrain above 3000 m ASL during most of the day. Both the ARI and ACI effect of aerosols tend to reduce the precipitation over the higher elevation above 3000 m ASL. The afternoon suppression of precipitation over the lowlands (below 2000 m ASL) is dominated by the ARI effect (Fig. 8c). It is noteworthy that, though the ACI effect of aerosols suppressed the nighttime (after 1800 LST) precipitation below 1000 m ASL, it extended the enhancement of precipitation to the higher elevation up to 3600 m ASL (Fig. 8d). This can be attributed to the microphysical effect of aerosols delaying the conversion of smaller cloud droplets to raindrops and enhancing the cloud lifetime, resulting in larger advection time for orographic clouds, increasing the downwind precipitation (Givati and Rosenfeld, 2004; Choudhury et al., 2019).

Variability in the amount of hourly precipitation increases from lower to higher altitudes (Fig. 2b), possibly due to the orographic feature associated with the abrupt change in the topographical gradient. To further investigate the response of elevational-dependent precipitation to the aerosols, we classified the mean precipitation intensity into heavy (> 1.04 mm/hr), moderate (between 0.42 and 1.04 mm/hr), and light (< 0.42 mm/hr) precipitation regime. A similar classification procedure has also been implemented by Sharma et al. (2020) for daily accumulated precipitation over Nepal Himalayas and for hourly precipitation over eastern China by Shao et al. (2022). Figures 9 and 10 show the differences and relative change (%) in elevation dependence of the precipitation regime in precipitation due to different effects of aerosols and reveal a contrasting elevational response. Though the ACI effect

slightly enhances the light precipitation below 1000 m ASL, the ARI effect dominates and monotonically suppresses

the mean light precipitation by 17% over the CenHim. Whereas the ACI effect enhances the precipitation below

3000 m ASL and shows a most prominent impact on moderate to heavy precipitation regimes. Contrasting to the

lower elevation, above 3000 m ASL, the ACI effect of aerosols suppressed all regimes of the precipitation intensity.

The elevation between 1000 and 3000 m ASL acts as the region below and above which the different intensity of

precipitation responds in the opposite direction to the effect of aerosols. The maximum increment (43%) in heavy

precipitation due to the aerosol effect occurred over the elevation bin between 200-400 m ASL (Fig. 10). Similarly,

the total precipitation was enhanced by 18% over the 200-400 m bin, while 5400-5600 m elevation experienced the

maximum reduction (21%). Below 2000 m ASL, due to the total effect of aerosols, the mean light precipitation is

suppressed by 19%, while moderate and heavy precipitation is enhanced by 3% and 12%, respectively. In contrast,

above 2000 m ASL, a significant suppression of all three categories of precipitation intensity is noticed with the

11% reduction in mean precipitation.

Likewise, in our results, Wu et al. (2018) showed that ACI suppressed the mountain top (> 2500 m ASL)

precipitation by 11% over the Sierra Nevada. Similarly, Napoli et al. (2022) also showed that the indirect effect of

aerosol resulted in suppressed summer precipitation in a polluted environment by 20% above 2000 m ASL of Great

Alpine mountainous region. In contrast to the enhanced precipitation in our result, these studies simulated the

suppressed precipitation even in the lower elevations of these mid-latitude mountainous region. This discrepancy

might be associated with the differences in the aerosol concentration from the heavily polluted upwind region of

IGP, enhanced moisture supply along with the monsoonal flow, and the steeper terrain of the Himalayas enhancing

the orographic forcing and convection compared to the Great Alpine and the Sierra Nevada.

In comparison to the CLEAN scenario, the elevational-dependent precipitation showed a similar response

in the diurnal cycle and spatial pattern to the increase in aerosols from CTL to D_AERO, besides the smaller

changes in the magnitude (not shown). The doubling in aerosols resulted in increased monthly mean heavy

precipitation below 2000 m ASL by 16% (4% higher compared to CTL run) and suppressed precipitation above the

2000 m ASL by 8% (similar to CTL run) compared to the CLEAN simulation. No significant differences were noted

in the change in light precipitation due to the doubling of aerosols. It might be related to the non-linear responses of

aerosol concentration to the convective intensity, microphysical, and dynamical effect (Fan et al., 2013; Chang et al.,

2015). Due to the stronger convection in the heavy precipitation regime, the potentiality of the aerosol getting

activated to cloud droplets increases in the presence of a higher aerosol concentration.

3.3 Aerosol Effect on Clouds

Figure 11a shows the CTL simulated diurnal-elevation of cloud fraction over the CenHim and resembles

the diurnal precipitation pattern. The higher elevation above 4000 meters has lower cloud coverage throughout the

day due to the limited atmospheric moisture reaching the higher elevation. The ACI effect increases the cloud

fraction over most of the elevation throughout the day due to the enhanced activation of aerosol as cloud droplets

(Fig. 11d). However, the ARI effect reduces the cloud coverage early in the morning below 2000 m ASL and the

suppression propagate higher in elevation during the afternoon and evening (Fig. 11c), which might be associated

with the weaker surface heating limiting the wind flows towards the slope of the mountain and afternoon orographic cloud development. Although there is a noisier and a less consistent diurnal-elevation relationship, the total aerosol effect is mostly that of enhancement of cloud cover. This result is consistent with long-term satellite retrieval of cloudiness during high aerosol concentration days (Adhikari and Mejia, 2021).

To further investigate the impact of anthropogenic aerosols on clouds and precipitation, the effect of aerosols on vertical velocity, LWP, and IWP is performed by dividing the terrain elevation below and above 2000 m ASL (Fig. 12), where the mean precipitation responded differently to the aerosols. Increased cloud coverage over the CenHim due to the aerosol effect is associated with the ACI effect resulting in enhanced cloud liquid water path (LWP) for all precipitation regimes (Fig. 12c-d). While ARI significantly contributes to the increase in ice water path (IWP; by 10%) below 2000 m ASL (Fig. 12e) along with the settle but upward 5% increase in mean vertical velocity (Fig. 12a). The ARI modulated increase in IWP below 2000 m ASL, where the amount of aerosol loading is higher, can be attributed to the warming of the atmosphere resulting in the evaporation of droplets and contributing to an increased upward moisture flux to the higher altitudes resulting in the formation of the ice. Other modeling studies have also reported an increment in the cloud ice water content due to the radiative heating effect of biomass burning (Liu et al., 2020) and dust aerosols (Dipu et al., 2013). While reduced IWP above 2000 m ASL due to ARI might be dominated by the surface cooling effect suppressing the cloud development. The minimal ACI effect in IWP is due to the lack of a model treating the activation of aerosol to ice nuclei.

The aerosol modulated vertical velocity below 2000 m ASL (Fig. 12a) suggests the convective strength is suppressed/enhanced for the light/heavy precipitation regime. Additionally, due to the total aerosols effect, the number of strong updraft events (mean vertical velocity higher than 0.5 ms^{-1}) increased by 10% below 2000 m ASL (except for the lowest elevational bin below 200 m ASL) and reduced by 11% above 2000 m ASL (not shown). Along with the stronger convection, the enhanced IWP and LWP indicate the invigoration of the cloud resulting in increased heavier precipitation below 2000 m ASL. In contrast, the suppressed convection and more aerosol activated as a higher number of smaller cloud droplets resulted in a nonprecipitating cloud suppressing the light precipitation over the entire CenHim. Figure S3 shows a clear difference in the vertically integrated cloud droplet number concentration between the simulations, with an increasing order from the CLEAN (lowest), CTL, and D_AERO (highest) simulations, in a similar order of aerosol concentration. Similarly, more aerosols are activated as cloud droplets over the lower elevational belt (<2000 m ASL) compared to relatively cleaner higher mountainous regions (> 2000 m ASL).

The suppression of light and enhanced heavy precipitation due to modulated convective strength by anthropogenic aerosol is consistent with a simulated study over eastern China by Shao et al. (2022). The increased precipitation over the foothills with an invigorated convection is consistent with our other study based on satellite retrieval over the southern slopes of the Central Himalayas (Adhikari and Mejia, 2021). Regardless of the meteorological forcing, Adhikari and Mejia (2021) showed a positive association of the aerosol loadings with the colder and deeper clouds resulting in enhanced precipitation. Also, another satellite-based study by Choudhury et al. (2020) suggests the higher aerosol loading with the increased moist static energy significantly contributed to the

424 extreme precipitation events over the Himalayan foothills. Similar to our findings, a case study by Adhikari and
425 Mejia (2022) also showed that long-range transported natural mineral dust aerosols modulated the microphysical
426 properties of clouds and enhanced the precipitation by 9.6% over the mid-mountainous (500-3000 m ASL) region of
427 Nepal Himalayas. However, our results indicate the contrasting response of precipitation at different elevational
428 bands to the increased aerosols. Similarly, during the spring season, Barman and Gokhale (2022) showed that the
429 atmospheric heating due to absorbing aerosol played a role in an increased influx of moisture with enhanced
430 instability over the lower terrain enhancing the rainfall while limiting the moisture over the higher terrain of
431 northeastern India.

3.4 Aerosol effect on Temperature and Radiation

433 Figure 13a shows the diurnal variation of decreasing temperature with increasing variability from low to
434 high elevations. The diurnal-elevation surface cooling effect due to anthropogenic aerosols during the daytime is
435 stronger throughout the elevational ranges (Fig. 13b-d). The daytime surface temperature cooling of -1.3 °C is likely
436 due to the total effect of aerosols over the terrain elevation above 4000 m ASL, with the ACI effect contributing to
437 most of the cooling (-1.1 °C). The daytime variation of change in surface temperature is consistent with all sky
438 downwelling shortwave radiation flux at the surface (hereafter SW; Fig. 14). Consistent with our results, over the
439 Great Alpine Region of Europe, Napoli et al. (2022) reported high-elevation strong daytime surface cooling related
440 to the enhancement of polluted orographic clouds with upslope winds blocking solar radiation. Another striking
441 feature in Fig. 14 is the smaller but significant nighttime surface temperature warming (+0.03 °C) above 2000 m
442 ASL, likely related to enhanced cloudiness (Fig. 11) favoring trapping of the longwave radiation (Fig. S4). Our
443 results indicate that the ACI effect of aerosols can significantly contribute to nighttime warming over the higher
444 elevation and contribute to warming by 0.08°C.

445 A prominent increase in minimum temperature in the recent decades over the higher elevation of the
446 Himalayan region has also been reported in previous studies (e.g., Dimri et al., 2022; Liu et al., 2009). The enhanced
447 nighttime minimum temperature has also been attributed to the enhanced cloud cover over the higher topographical
448 elevation (Rangwala and Miller, 2012; Liu et al., 2009) and increased cloud liquid water path due to the aerosol
449 indirect effect over East Asia (Huang et al., 2006b). Notably, the lack of aerosol snow interaction and deposition of
450 light-absorbing aerosols on the snow surfaces in our simulation can add uncertainties to simulated temperature
451 differences. The deposition of absorbing aerosol on snow has a crucial impact on the snow darkening effect, the
452 surface temperature, and the radiative forcing of the snowcapped Himalayan region (Qian et al., 2015; Sarangi et al.,
453 2019). Wu et al. (2018) showed that the inclusion of aerosol snow interaction in the model simulation resulted in a
454 significant increase in the surface temperature of the snowcapped mountain of Sierra Nevada.

455 Figure 14 (a-c) shows aerosol total, ARI, and ACI effects on the diurnal-elevational variation of all sky
456 SW, highlighting the stronger reduction of SW due to the aerosol effect at high elevations. The terrain elevation
457 above 4000 m ASL noted the reduction of SW by -82.8 W m^{-2}, and most contribution is from the ACI effect of
458 aerosols (Fig. 14c). The negative shortwave radiative perturbation at the surface due to the ACI effect is stronger
459 and can be attributed to the higher cloud liquid water path (LWP) and enhanced cloud albedo due to more aerosols

460 activated as condensation nuclei (Twomey, 1977). The stronger reduction of mid-day all sky SW over the higher

461 elevation compared to the lower elevation is due to the ACI effect, which results in the formation of persistent

462 polluted orographic clouds along with the upslope wind due to the ACI effect. A distinct difference in the impact of

463 an elevational gradient in the SW for the clear sky (excluding cloud; Fig. 14 d-f) and all sky (including cloud)

464 conditions are also noted. The reduction of the clear sky SW due to the aerosols at the terrain elevation below 1200

465 meters is stronger (-21 WM^{-2}), where the aerosol loadings are higher and is dominated by the ARI effect of aerosols.

466 The higher elevation above 4000 m ASL experienced the smaller negative perturbation of clear sky SW radiation (>

467 -5 Wm^{-2}). This change in clear sky SW in a relatively polluted environment at a higher elevation is consistent with a

468 study by Marcq et al. (2010) reporting a similar change near the base camp (5079 m ASL) of Mount Everest.

469 4 Conclusions

470 The presence of steep mountainous terrain and orographic distribution drives the very complex and non-

471 linear precipitation system over the Central Himalayan region. Despite the importance of the hydrological processes

472 of the Himalayas, research studying the impact of aerosols in modulating the elevation-dependent precipitation over

473 the Central Himalayas using cloud-resolving numerical simulation has not been performed until now.

474 The first monsoonal month of 2013 (June 14 to July 15) is simulated using a high-resolution cloud-

475 resolving WRF-Chem numerical modeling to understand the impact of aerosols on the elevation-dependent

476 precipitation over the very complex terrain of the Central Himalayan region. In addition to explicitly resolving the

477 cloud evolution, the detailed topographical representation by the cloud-resolving scale model better simulates the

478 emission and transport processes of aerosols. So, the cloud-resolving simulation is important to provide better

479 insight and quantify the impact of aerosol on elevation-dependent precipitation over complex terrain. In addition to

480 CTL (baseline) simulation, two different numerical experiments were performed, similar to the CTL run but turning

481 off the aerosol radiation feedback and reducing the anthropogenic aerosols to 10% of CTL. The comparison between

482 the simulation experiments allowed us to assess and discuss the relative impact of aerosol radiation and cloud

483 interaction on the diurnal variation and different regimes of elevation-dependent precipitation and temperature.

484 Figure 15 illustrates the summaries of our main conclusions. We showed that the total effect of

485 anthropogenic aerosols cooled the daytime surface monotonically from lower to higher elevations. The higher

486 elevation showed a strong diurnal variation in surface temperature, with a strong cooling above 4000 m ASL during

487 the daytime (by -1.3°C) and above 2000m ASL, nighttime warming (+0.03 °C). The increased LWP and cloud

488 coverage during daytime with higher aerosol concentration is attributed to the reduced SW and daytime temperature,

489 while nighttime warming is due to the trapping of longwave radiation.

490 Our modeling experiment showed an altitudinal differential response by precipitation (intensity and diurnal

491 variation) to the anthropogenic aerosols. The mid elevation range, generally between 1000 and 3000 m ASL, act as a

492 transition layer where the diurnal variation and various intensity of precipitation respond differently to the ARI,

493 ACI, and total effect of aerosols. The total effect of aerosols tends to enhance the precipitation below 2000 m ASL,

494 while a significant reduction of precipitation occurs above 2000 m ASL with a dominating contribution from the

495   ACI effect. The total effect of aerosols reduced the mean light precipitation by 17%. However, along with the
496   stronger convection below 2000 m ASL the ACI effect dominated and resulted in the enhancement of the heavy
497   precipitation by 12%, contrasting to the reduction by 8% over the higher elevations. The result of our study can have
498   a broader impact and suggests that enhanced heavy precipitation over the elevation below 2000 m ASL can increase
499   the risk for extreme events (floods and landslides), while the suppressed high elevation precipitation can be critical
500   for the regional supply of water resources (Immerzeel et al., 2010).

501   The numerical simulation implemented in this study has several limitations. Due to the limited
502   computational resources, few sensitivity simulations were performed to assess the precipitation response to the
503   different effects of aerosols. Lack of complete effects of aerosols in the model, such as INP activation and formation
504   of secondary organic aerosols, can induce and add up the biases in our result. In this simulation, the contribution
505   from the impact of aerosol-surface-snow interaction is not included, which can also play a part in modulating the
506   mountain top surface temperature and orographic precipitation (Wu et al., 2018). The SNICAR (Snow, Ice, and
507   Aerosol Radiation) model (Flanner et al., 2007), capable of simulating the snow surface albedo and aerosol radiative
508   effect in snow, can be coupled with the WRF-Chem to study the aerosol-snow-interaction (Zhao et al., 2014). Also,
509   it is noted that there are biases in assessing the ACI effect associated with the presence of 10% aerosols and
510   contribution from the fire and biogenic emissions in the CLEAN scenario. Furthermore, the 3 km grid sizes might be
511   relatively coarser to resolve the orographic forcing and mountain-valley circulation of the steep and complex
512   topography of the Himalayas. Due to the inhomogeneity in the aerosol distribution over the complex topography,
513   improved emission inventory with diurnal distribution will help advance the current understanding of the diurnal
514   impact of aerosols on temperature distribution and the convective/precipitation process. There is a need for
515   continuous data collection from a denser distribution of observational networks (e.g., AERONET and weather
516   stations) with more meteorological variables along the elevational transect of the Himalayan topography, especially
517   over the high elevation region. It not only quantifies the long-term trend and pattern of the sensitive regions but also
518   helps evaluate and constrain numerical modeling studies in complex terrain.

519   Despite some biases and existing uncertainties in the model, our results underline the noticeable impact of
520   aerosols on elevational-dependent precipitation. Though we simulated only the first month of the monsoon, our
521   results indicate that the anthropogenic aerosol plays a significant role in enhancing (suppressing) the low elevation
522   (high elevation) precipitation. The underlying aerosol-precipitation-elevation relationships may vary during different
523   states of the monsoon as the abundance of aerosols tends to decrease during the mature to demise stage of the
524   monsoon. Hence, longer term simulations with a complete parametrization scheme to include the ice phase aerosol-
525   cloud interaction and aerosol-snow interaction pathways and better emission inventory with characterization are
526   warranted to deepen our understanding of such elevational dependence. This could be the future scope and extension
527   of this study.

528

Code/Data Availability

The MODIS data are available through the following link: https://ladsweb.modaps.eosdis.nasa.gov/search/order

The IMERG data are available through the following link: https://disc.gsfc.nasa.gov/

The DHM rain gauge station precipitation data can be requested through the following link:
https://www.dhm.gov.np/request-data

The upper air sounding data are available through the following link:
http://weather.uwyo.edu/upperair/sounding.html

The AERONET data are available through the following link: https://aeronet.gsfc.nasa.gov/cgi-bin/webtool_aod_v3

The WRF-Chem model code is distributed by NCAR: https://github.com/wrf-model/WRF/releases

Author contribution

PA and JM designed the numerical experiments, and PA performed the simulations. PA and JM performed the analysis and interpreted the results. PA prepared the original draft of the manuscript with equal contributions from JM.

Competing interests

The authors declare that they have no conflict of interest.

Acknowledgements

The authors would like to thank the Division of Atmospheric Sciences, Desert Research Institute (DRI), and the University of Nevada Reno for supporting this research. The Division of Atmospheric Sciences partially funds Dr. Mejia at DRI. We also thank the assistantship support for Mr. Adhikari from the DRI and through Dr. Mejia's DRI Institute Project Assignment funds. We would like to acknowledge high-performance computing support from Cheyenne (doi:10.5065/D6RX99HX) provided by NCAR's Computational and Information Systems Laboratory, sponsored by the National Science Foundation. We also thank NASA for providing the IMERG, AERONET, and MERRA2 data. We also thank the Department of Hydrology and Meteorology Nepal for providing the precipitation data from the rain gauge stations. We would like to acknowledge Dr. Douglas Lowe (University of Manchester) and the Atmospheric Chemistry Observations and Modeling Lab (ACOM) of NCAR for providing the WRF-Chem preprocessor tool.

References

Abdul-Razzak, H. and Ghan, S. J.: A parameterization of aerosol activation 3. Sectional representation, Journal of Geophysical Research: Atmospheres, 107, AAC 1-1-AAC 1-6, https://doi.org/10.1029/2001JD000483, 2002.

Ackerman, A. S., Toon, O. B., Stevens, D. E., Heymsfield, A. J., Ramanathan, V., and Welton, E. J.: Reduction of Tropical Cloudiness by Soot, Science, https://doi.org/10.1126/science.288.5468.1042, 2000.

Adhikari, P. and Mejia, J. F.: Influence of aerosols on clouds, precipitation and freezing level height over the foothills of the Himalayas during the Indian summer monsoon, Clim Dyn, https://doi.org/10.1007/s00382-021-05710-2, 2021.

Adhikari, P. and Mejia, J. F.: Impact of transported dust aerosols on precipitation over the Nepal Himalayas using convection-permitting WRF-Chem simulation, Atmospheric Environment: X, 15, 100179, https://doi.org/10.1016/j.aeaoa.2022.100179, 2022.

Albrecht, B. A.: Aerosols, Cloud Microphysics, and Fractional Cloudiness, Science, 245, 1227–1230, https://doi.org/10.1126/science.245.4923.1227, 1989.

Andreae, M. O. and Rosenfeld, D.: Aerosol–cloud–precipitation interactions. Part 1. The nature and sources of cloud-active aerosols, Earth-Science Reviews, 89, 13–41, https://doi.org/10.1016/j.earscirev.2008.03.001, 2008.

Andreae, M. O., Rosenfeld, D., Artaxo, P., Costa, A. A., Frank, G. P., Longo, K. M., and Silva-Dias, M. A. F.: Smoking rain clouds over the Amazon, Science, 303, 1337–1342, https://doi.org/10.1126/science.1092779, 2004.

Archer-Nicholls, S., Lowe, D., Schultz, D. M., and McFiggans, G.: Aerosol–radiation–cloud interactions in a regional coupled model: the effects of convective parameterisation and resolution, Atmos. Chem. Phys., 16, 5573–5594, https://doi.org/10.5194/acp-16-5573-2016, 2016.

Arulraj, M. and Barros, A. P.: Improving quantitative precipitation estimates in mountainous regions by modelling low-level seeder-feeder interactions constrained by Global Precipitation Measurement Dual-frequency Precipitation Radar measurements, Remote Sensing of Environment, 231, 111213, https://doi.org/10.1016/j.rse.2019.111213, 2019.

Barman, N. and Gokhale, S.: Aerosol influence on the pre-monsoon rainfall mechanisms over North-East India: A WRF-Chem study, Atmospheric Research, 268, 106002, https://doi.org/10.1016/j.atmosres.2021.106002, 2022.

Baró, R., Jiménez-Guerrero, P., Balzarini, A., Curci, G., Forkel, R., Grell, G., Hirtl, M., Honzak, L., Langer, M., Pérez, J. L., Pirovano, G., San José, R., Tuccella, P., Werhahn, J., and Žabkar, R.: Sensitivity analysis of the microphysics scheme in WRF-Chem contributions to AQMEII phase 2, Atmospheric Environment, 115, 620–629, https://doi.org/10.1016/j.atmosenv.2015.01.047, 2015.

Bradley, R. S., Keimig, F. T., Diaz, H. F., and Hardy, D. R.: Recent changes in freezing level heights in the Tropics with implications for the deglacierization of high mountain regions, Geophysical Research Letters, 36, https://doi.org/10.1029/2009GL037712, 2009.

Buchholz, R. R., Emmons, L. K., Tilmes, S., and The CESM2 Development Team: CESM2. 1/CAM-chem instantaneous output for boundary conditions, UCAR/NCAR-Atmospheric Chemistry Observations and Modeling Laboratory, https://doi.org/10.5065/NMP7-EP60, 2019.

Cao, Q., Painter, T. H., Currier, W. R., Lundquist, J. D., and Lettenmaier, D. P.: Estimation of Precipitation over the OLYMPEX Domain during Winter 2015/16, Journal of Hydrometeorology, 19, 143–160, https://doi.org/10.1175/JHM-D-17-0076.1, 2018.

599 Chang, D., Cheng, Y., Reutter, P., Trentmann, J., Burrows, S. M., Spichtinger, P., Nordmann, S., Andreae, M. O.,
600 Pöschl, U., and Su, H.: Comprehensive mapping and characteristic regimes of aerosol effects on the formation and
601 evolution of pyro-convective clouds, Atmospheric Chemistry and Physics, 15, 10325–10348,
602 https://doi.org/10.5194/acp-15-10325-2015, 2015.

603 Chapman, E. G., Jr, W. I. G., Easter, R. C., Barnard, J. C., Ghan, S. J., Pekour, M. S., and Fast, J. D.: Coupling
604 aerosol-cloud-radiative processes in the WRF-Chem model: Investigating the radiative impact of elevated point
605 sources, Atmos. Chem. Phys., 20, 2009.

606 Cho, C., Li, R., Wang, S.-Y., Yoon, J.-H., and Gillies, R. R.: Anthropogenic footprint of climate change in the June
607 2013 northern India flood, Clim Dyn, 46, 797–805, https://doi.org/10.1007/s00382-015-2613-2, 2016.

608 Choudhury, G., Tyagi, B., Singh, J., Sarangi, C., and Tripathi, S. N.: Aerosol-orography-precipitation – A critical
609 assessment, Atmospheric Environment, 214, 116831, https://doi.org/10.1016/j.atmosenv.2019.116831, 2019.

610 Choudhury, G., Tyagi, B., Vissa, N. K., Singh, J., Sarangi, C., Tripathi, S. N., and Tesche, M.: Aerosol-enhanced
611 high precipitation events near the Himalayan foothills, Atmospheric Chemistry and Physics, 20, 15389–15399,
612 https://doi.org/10.5194/acp-20-15389-2020, 2020.

613 Dey, S. and Di Girolamo, L.: A decade of change in aerosol properties over the Indian subcontinent, Geophysical
614 Research Letters, 38, https://doi.org/10.1029/2011GL048153, 2011.

615 Dhital, S., Kaplan, M. L., Orza, J. a. G., and Fiedler, S.: The Extreme North African Haboob in October 2008: High-
616 Resolution Simulation of Organized Moist Convection in the Lee of the Atlas, Dust Recirculation and Poleward
617 Transport, Journal of Geophysical Research: Atmospheres, 127, e2021JD035858,
618 https://doi.org/10.1029/2021JD035858, 2022.

619 DHM Nepal: Monsoon onset and withdrawal date information.
620 http://www.dhm.gov.np/uploads/climatic/841739888monsoon%20onset%20n%20withdrawal%20English_6%20Jun
621 e%202022.pdf, 2022.

622 Dimri, A. P., Palazzi, E., and Daloz, A. S.: Elevation dependent precipitation and temperature changes over Indian
623 Himalayan region, Clim Dyn, https://doi.org/10.1007/s00382-021-06113-z, 2022.

624 Dipu, S., Prabha, T. V., Pandithurai, G., Dudhia, J., Pfister, G., Rajesh, K., and Goswami, B. N.: Impact of elevated
625 aerosol layer on the cloud macrophysical properties prior to monsoon onset, Atmospheric Environment, 70, 454–
626 467, https://doi.org/10.1016/j.atmosenv.2012.12.036, 2013.

627 Eidhammer, T., Barth, M. C., Petters, M. D., Wiedinmyer, C., and Prenni, A. J.: Aerosol microphysical impact on
628 summertime convective precipitation in the Rocky Mountain region, Journal of Geophysical Research:
629 Atmospheres, 119, 11,709-11,728, https://doi.org/10.1002/2014JD021883, 2014.

630 Emmons, L. K., Schwantes, R. H., Orlando, J. J., Tyndall, G., Kinnison, D., Lamarque, J.-F., Marsh, D., Mills, M.
631 J., Tilmes, S., Bardeen, C., Buchholz, R. R., Conley, A., Gettelman, A., Garcia, R., Simpson, I., Blake, D. R.,
632 Meinardi, S., and Pétron, G.: The Chemistry Mechanism in the Community Earth System Model Version 2
633 (CESM2), Journal of Advances in Modeling Earth Systems, 12, e2019MS001882,
634 https://doi.org/10.1029/2019MS001882, 2020.

635 Fan, J., Zhang, R., Li, G., and Tao, W.-K.: Effects of aerosols and relative humidity on cumulus clouds, Journal of
636 Geophysical Research: Atmospheres, 112, https://doi.org/10.1029/2006JD008136, 2007.

637 Fan, J., Leung, L. R., Rosenfeld, D., Chen, Q., Li, Z., Zhang, J., and Yan, H.: Microphysical effects determine
638 macrophysical response for aerosol impacts on deep convective clouds, PNAS, 110, E4581–E4590,
639 https://doi.org/10.1073/pnas.1316830110, 2013.

640   Fan, J., Rosenfeld, D., Yang, Y., Zhao, C., Leung, L. R., and Li, Z.: Substantial contribution of anthropogenic air
641   pollution to catastrophic floods in Southwest China, Geophysical Research Letters, 42, 6066–6075,
642   https://doi.org/10.1002/2015GL064479, 2015.

643   Fan, J., Leung, L. R., Rosenfeld, D., and DeMott, P. J.: Effects of cloud condensation nuclei and ice nucleating
644   particles on precipitation processes and supercooled liquid in mixed-phase orographic clouds, Atmospheric
645   Chemistry and Physics, 17, 1017–1035, https://doi.org/10.5194/acp-17-1017-2017, 2017.

646   Fast, J. D., Gustafson, W. I., Easter, R. C., Zaveri, R. A., Barnard, J. C., Chapman, E. G., Grell, G. A., and Peckham,
647   S. E.: Evolution of ozone, particulates, and aerosol direct radiative forcing in the vicinity of Houston using a fully
648   coupled meteorology-chemistry-aerosol model, Journal of Geophysical Research: Atmospheres, 111,
649   https://doi.org/10.1029/2005JD006721, 2006.

650   Flanner, M. G., Zender, C. S., Randerson, J. T., and Rasch, P. J.: Present-day climate forcing and response from
651   black carbon in snow, Journal of Geophysical Research: Atmospheres, 112, https://doi.org/10.1029/2006JD008003,
652   2007.

653   Fujinami, H., Fujita, K., Takahashi, N., Sato, T., Kanamori, H., Sunako, S., and Kayastha, R. B.: Twice-Daily
654   Monsoon Precipitation Maxima in the Himalayas Driven by Land Surface Effects, Journal of Geophysical Research:
655   Atmospheres, 126, e2020JD034255, https://doi.org/10.1029/2020JD034255, 2021.

656   Gery, M. W., Whitten, G. Z., Killus, J. P., and Dodge, M. C.: A photochemical kinetics mechanism for urban and
657   regional scale computer modeling, Journal of Geophysical Research: Atmospheres, 94, 12925–12956,
658   https://doi.org/10.1029/JD094iD10p12925, 1989.

659   Ghimire, S., Choudhary, A., and Dimri, A. P.: Assessment of the performance of CORDEX-South Asia experiments
660   for monsoonal precipitation over the Himalayan region during present climate: part I, Clim Dyn, 50, 2311–2334,
661   https://doi.org/10.1007/s00382-015-2747-2, 2018.

662   Givati, A. and Rosenfeld, D.: Quantifying Precipitation Suppression Due to Air Pollution, Journal of Applied
663   Meteorology and Climatology, 43, 1038–1056, https://doi.org/10.1175/1520-
664   0450(2004)043<1038:QPSDTA>2.0.CO;2, 2004.

665   Govardhan, G., Nanjundiah, R. S., Satheesh, S. K., Krishnamoorthy, K., and Kotamarthi, V. R.: Performance of
666   WRF-Chem over Indian region: Comparison with measurements, J Earth Syst Sci, 124, 875–896,
667   https://doi.org/10.1007/s12040-015-0576-7, 2015.

668   Grell, G., Freitas, S. R., Stuefer, M., and Fast, J.: Inclusion of biomass burning in WRF-Chem: impact of wildfires
669   on weather forecasts, Atmospheric Chemistry and Physics, 11, 5289–5303, https://doi.org/10.5194/acp-11-5289-
670   2011, 2011.

671   Grell, G. A. and Dévényi, D.: A generalized approach to parameterizing convection combining ensemble and data
672   assimilation techniques, Geophysical Research Letters, 29, 38-1-38–4, https://doi.org/10.1029/2002GL015311,
673   2002.

674   Grell, G. A., Peckham, S. E., Schmitz, R., McKeen, S. A., Frost, G., Skamarock, W. C., and Eder, B.: Fully coupled
675   "online" chemistry within the WRF model, Atmospheric Environment, 39, 6957–6975,
676   https://doi.org/10.1016/j.atmosenv.2005.04.027, 2005.

677   Guenther, A., Karl, T., Harley, P., Wiedinmyer, C., Palmer, P. I., and Geron, C.: Estimates of global terrestrial
678   isoprene emissions using MEGAN (Model of Emissions of Gases and Aerosols from Nature), Atmospheric
679   Chemistry and Physics, 6, 3181–3210, https://doi.org/10.5194/acp-6-3181-2006, 2006.

680   Guenther, A. B., Jiang, X., Heald, C. L., Sakulyanontvittaya, T., Duhl, T., Emmons, L. K., and Wang, X.: The
681   Model of Emissions of Gases and Aerosols from Nature version 2.1 (MEGAN2.1): an extended and updated

682 framework for modeling biogenic emissions, Geoscientific Model Development, 5, 1471–1492,
683 https://doi.org/10.5194/gmd-5-1471-2012, 2012.

684 Hallquist, M., Wenger, J. C., Baltensperger, U., Rudich, Y., Simpson, D., Claeys, M., Dommen, J., Donahue, N. M.,
685 George, C., Goldstein, A. H., Hamilton, J. F., Herrmann, H., Hoffmann, T., Iinuma, Y., Jang, M., Jenkin, M. E.,
686 Jimenez, J. L., Kiendler-Scharr, A., Maenhaut, W., McFiggans, G., Mentel, T. F., Monod, A., Prévôt, A. S. H.,
687 Seinfeld, J. H., Surratt, J. D., Szmigielski, R., and Wildt, J.: The formation, properties and impact of secondary
688 organic aerosol: current and emerging issues, Atmospheric Chemistry and Physics, 9, 5155–5236,
689 https://doi.org/10.5194/acp-9-5155-2009, 2009.

690 Hansen, J., Sato, M., and Ruedy, R.: Radiative forcing and climate response, Journal of Geophysical Research:
691 Atmospheres, 102, 6831–6864, https://doi.org/10.1029/96JD03436, 1997.

692 Haywood, J. and Boucher, O.: Estimates of the direct and indirect radiative forcing due to tropospheric aerosols: A
693 review, Reviews of Geophysics, 38, 513–543, https://doi.org/10.1029/1999RG000078, 2000.

694 Hersbach, H., Bell, B., Berrisford, P., Hirahara, S., Horányi, A., Muñoz-Sabater, J., Nicolas, J., Peubey, C., Radu,
695 R., Schepers, D., Simmons, A., Soci, C., Abdalla, S., Abellan, X., Balsamo, G., Bechtold, P., Biavati, G., Bidlot, J.,
696 Bonavita, M., De Chiara, G., Dahlgren, P., Dee, D., Diamantakis, M., Dragani, R., Flemming, J., Forbes, R.,
697 Fuentes, M., Geer, A., Haimberger, L., Healy, S., Hogan, R. J., Hólm, E., Janisková, M., Keeley, S., Laloyaux, P.,
698 Lopez, P., Lupu, C., Radnoti, G., de Rosnay, P., Rozum, I., Vamborg, F., Villaume, S., and Thépaut, J.-N.: The
699 ERA5 global reanalysis, Quarterly Journal of the Royal Meteorological Society, 146, 1999–2049,
700 https://doi.org/10.1002/qj.3803, 2020.

701 Hong, S.-Y., Noh, Y., and Dudhia, J.: A New Vertical Diffusion Package with an Explicit Treatment of Entrainment
702 Processes, Mon. Wea. Rev., 134, 2318–2341, https://doi.org/10.1175/MWR3199.1, 2006.

703 Huang, J., Lin, B., Minnis, P., Wang, T., Wang, X., Hu, Y., Yi, Y., and Ayers, J. K.: Satellite-based assessment of
704 possible dust aerosols semi-direct effect on cloud water path over East Asia, Geophysical Research Letters, 33,
705 https://doi.org/10.1029/2006GL026561, 2006a.

706 Huang, Y., Dickinson, R. E., and Chameides, W. L.: Impact of aerosol indirect effect on surface temperature over
707 East Asia, Proceedings of the National Academy of Sciences, 103, 4371–4376,
708 https://doi.org/10.1073/pnas.0504428103, 2006b.

709 Huffman, G. J., Stocker, E. F., Bolvin, D. T., Nelkin, E. J., and Tan, J.: GPM IMERG Early Precipitation L3 Half
710 Hourly 0.1 degree x 0.1 degree V06, Goddard Earth Sciences Data and Information Services Center (GES DISC),
711 Greenbelt, MD, https://doi.org/10.5067/GPM/IMERG/3B-HH-E/06, 2019.

712 Iacono, M. J., Delamere, J. S., Mlawer, E. J., Shephard, M. W., Clough, S. A., and Collins, W. D.: Radiative forcing
713 by long-lived greenhouse gases: Calculations with the AER radiative transfer models, Journal of Geophysical
714 Research: Atmospheres, 113, https://doi.org/10.1029/2008JD009944, 2008.

715 Immerzeel, W. W., van Beek, L. P. H., and Bierkens, M. F. P.: Climate Change Will Affect the Asian Water
716 Towers, Science, 328, 1382–1385, https://doi.org/10.1126/science.1183188, 2010.

717 IPCC: Climate change 2013: The Physical Science Basis: Working Group I Contribution to the Fifth Assessment
718 Report of the Intergovernmental Panel on Climate, Cambridge University Press, 1553 pp., 2013.

719 Janssens-Maenhout, G., Crippa, M., Guizzardi, D., Dentener, F., Muntean, M., Pouliot, G., Keating, T., Zhang, Q.,
720 Kurokawa, J., Wankmüller, R., Denier van der Gon, H., Kuenen, J. J. P., Klimont, Z., Frost, G., Darras, S., Koffi,
721 B., and Li, M.: HTAP_v2.2: a mosaic of regional and global emission grid maps for 2008 and 2010 to study
722 hemispheric transport of air pollution, Atmospheric Chemistry and Physics, 15, 11411–11432,
723 https://doi.org/10.5194/acp-15-11411-2015, 2015.

724 Ji, Z., Kang, S., Cong, Z., Zhang, Q., and Yao, T.: Simulation of carbonaceous aerosols over the Third Pole and
725 adjacent regions: distribution, transportation, deposition, and climatic effects, Clim Dyn, 45, 2831–2846,
726 https://doi.org/10.1007/s00382-015-2509-1, 2015.

727 Kang, S., Zhang, Q., Qian, Y., Ji, Z., Li, C., Cong, Z., Zhang, Y., Guo, J., Du, W., Huang, J., You, Q., Panday, A.
728 K., Rupakheti, M., Chen, D., Gustafsson, Ö., Thiemens, M. H., and Qin, D.: Linking atmospheric pollution to
729 cryospheric change in the Third Pole region: current progress and future prospects, Natl Sci Rev, 6, 796–809,
730 https://doi.org/10.1093/nsr/nwz031, 2019.

731 Kant, S., Panda, J., Rao, P., Sarangi, C., and Ghude, S. D.: Study of aerosol-cloud-precipitation-meteorology
732 interaction during a distinct weather event over the Indian region using WRF-Chem, Atmospheric Research, 247,
733 105144, https://doi.org/10.1016/j.atmosres.2020.105144, 2021.

734 Kaul, D. S., Gupta, T., Tripathi, S. N., Tare, V., and Collett, J. L.: Secondary Organic Aerosol: A Comparison
735 between Foggy and Nonfoggy Days, Environ. Sci. Technol., 45, 7307–7313, https://doi.org/10.1021/es201081d,
736 2011.

737 Khain, A., Lynn, B., and Shpund, J.: High resolution WRF simulations of Hurricane Irene: Sensitivity to aerosols
738 and choice of microphysical schemes, Atmospheric Research, 167, 129–145,
739 https://doi.org/10.1016/j.atmosres.2015.07.014, 2016.

740 Koren, I., Kaufman, Y. J., Rosenfeld, D., Remer, L. A., and Rudich, Y.: Aerosol invigoration and restructuring of
741 Atlantic convective clouds, Geophysical Research Letters, 32, https://doi.org/10.1029/2005GL023187, 2005.

742 Kumar, M., Parmar, K. S., Kumar, D. B., Mhawish, A., Broday, D. M., Mall, R. K., and Banerjee, T.: Long-term
743 aerosol climatology over Indo-Gangetic Plain: Trend, prediction and potential source fields, Atmospheric
744 Environment, 180, 37–50, https://doi.org/10.1016/j.atmosenv.2018.02.027, 2018.

745 Lau, K. M., Kim, M. K., and Kim, K. M.: Asian summer monsoon anomalies induced by aerosol direct forcing: the
746 role of the Tibetan Plateau, Clim Dyn, 26, 855–864, https://doi.org/10.1007/s00382-006-0114-z, 2006.

747 Lau, W. K. M., Kim, K.-M., Shi, J.-J., Matsui, T., Chin, M., Tan, Q., Peters-Lidard, C., and Tao, W. K.: Impacts of
748 aerosol–monsoon interaction on rainfall and circulation over Northern India and the Himalaya Foothills, Clim Dyn,
749 49, 1945–1960, https://doi.org/10.1007/s00382-016-3430-y, 2017.

750 Li, Z., Lau, W. K.-M., Ramanathan, V., Wu, G., Ding, Y., Manoj, M. G., Liu, J., Qian, Y., Li, J., Zhou, T., Fan, J.,
751 Rosenfeld, D., Ming, Y., Wang, Y., Huang, J., Wang, B., Xu, X., Lee, S.-S., Cribb, M., Zhang, F., Yang, X., Zhao,
752 C., Takemura, T., Wang, K., Xia, X., Yin, Y., Zhang, H., Guo, J., Zhai, P. M., Sugimoto, N., Babu, S. S., and
753 Brasseur, G. P.: Aerosol and monsoon climate interactions over Asia, Reviews of Geophysics, 54, 866–929,
754 https://doi.org/10.1002/2015RG000500, 2016.

755 Liu, L., Cheng, Y., Wang, S., Wei, C., Pöhlker, M. L., Pöhlker, C., Artaxo, P., Shrivastava, M., Andreae, M. O.,
756 Pöschl, U., and Su, H.: Impact of biomass burning aerosols on radiation, clouds, and precipitation over the Amazon:
757 relative importance of aerosol–cloud and aerosol–radiation interactions, Atmospheric Chemistry and Physics, 20,
758 13283–13301, https://doi.org/10.5194/acp-20-13283-2020, 2020.

759 Liu, X., Cheng, Z., Yan, L., and Yin, Z.-Y.: Elevation dependency of recent and future minimum surface air
760 temperature trends in the Tibetan Plateau and its surroundings, Global and Planetary Change, 68, 164–174,
761 https://doi.org/10.1016/j.gloplacha.2009.03.017, 2009.

762 Liu, Z., Gao, Y., and Zhang, G.: How well can a convection-permitting-modelling improve the simulation of
763 summer precipitation diurnal cycle over the Tibetan Plateau?, Clim Dyn, 58, 3121–3138,
764 https://doi.org/10.1007/s00382-021-06090-3, 2022.

765 Lynn, E., Cuthbertson, A., He, M., Vasquez, J. P., Anderson, M. L., Coombe, P., Abatzoglou, J. T., and Hatchett, B.
766 J.: Technical note: Precipitation-phase partitioning at landscape scales to regional scales, Hydrology and Earth
767 System Sciences, 24, 5317–5328, https://doi.org/10.5194/hess-24-5317-2020, 2020.

768 Mahowald, N., Ward, D. S., Kloster, S., Flanner, M. G., Heald, C. L., Heavens, N. G., Hess, P. G., Lamarque, J.-F.,
769 and Chuang, P. Y.: Aerosol Impacts on Climate and Biogeochemistry, Annual Review of Environment and
770 Resources, 36, 45–74, https://doi.org/10.1146/annurev-environ-042009-094507, 2011.

771 Manoj, M. G., Lee, S.-S., and Li, Z.: Competing aerosol effects in triggering deep convection over the Indian
772 Region, Clim Dyn, 56, 1815–1835, https://doi.org/10.1007/s00382-020-05561-3, 2021.

773 Marcq, S., Laj, P., Roger, J. C., Villani, P., Sellegri, K., Bonasoni, P., Marinoni, A., Cristofanelli, P., Verza, G. P.,
774 and Bergin, M.: Aerosol optical properties and radiative forcing in the high Himalaya based on measurements at the
775 Nepal Climate Observatory-Pyramid site (5079 m a.s.l.), Atmos. Chem. Phys., 10, 5859–5872,
776 https://doi.org/10.5194/acp-10-5859-2010, 2010.

777 Matin, M. A., Chitale, V. S., Murthy, M. S. R., Uddin, K., Bajracharya, B., and Pradhan, S.: Understanding forest
778 fire patterns and risk in Nepal using remote sensing, geographic information system and historical fire data, Int. J.
779 Wildland Fire, 26, 276–286, https://doi.org/10.1071/WF16056, 2017.

780 Morrison, H., Thompson, G., and Tatarskii, V.: Impact of Cloud Microphysics on the Development of Trailing
781 Stratiform Precipitation in a Simulated Squall Line: Comparison of One- and Two-Moment Schemes, Mon. Wea.
782 Rev., 137, 991–1007, https://doi.org/10.1175/2008MWR2556.1, 2009.

783 Mues, A., Lauer, A., Lupascu, A., Rupakheti, M., Kuik, F., and Lawrence, M. G.: WRF and WRF-Chem v3.5.1
784 simulations of meteorology and black carbon concentrations in the Kathmandu Valley, Geoscientific Model
785 Development, 11, 2067–2091, https://doi.org/10.5194/gmd-11-2067-2018, 2018.

786 Nair, V. S., Solmon, F., Giorgi, F., Mariotti, L., Babu, S. S., and Moorthy, K. K.: Simulation of South Asian
787 aerosols for regional climate studies, Journal of Geophysical Research: Atmospheres, 117,
788 https://doi.org/10.1029/2011JD016711, 2012.

789 Napoli, A., Crespi, A., Ragone, F., Maugeri, M., and Pasquero, C.: Variability of orographic enhancement of
790 precipitation in the Alpine region, Sci Rep, 9, 13352, https://doi.org/10.1038/s41598-019-49974-5, 2019.

791 Napoli, A., Desbiolles, F., Parodi, A., and Pasquero, C.: Aerosol indirect effects in complex-orography areas: a
792 numerical study over the Great Alpine Region, Atmospheric Chemistry and Physics, 22, 3901–3909,
793 https://doi.org/10.5194/acp-22-3901-2022, 2022.

794 Palazzi, E., von Hardenberg, J., and Provenzale, A.: Precipitation in the Hindu-Kush Karakoram Himalaya:
795 Observations and future scenarios, Journal of Geophysical Research: Atmospheres, 118, 85–100,
796 https://doi.org/10.1029/2012JD018697, 2013.

797 Palazzi, E., Filippi, L., and von Hardenberg, J.: Insights into elevation-dependent warming in the Tibetan Plateau-
798 Himalayas from CMIP5 model simulations, Clim Dyn, 48, 3991–4008, https://doi.org/10.1007/s00382-016-3316-z,
799 2017.

800 Parajuli, S. P., Stenchikov, G. L., Ukhov, A., and Kim, H.: Dust Emission Modeling Using a New High-Resolution
801 Dust Source Function in WRF-Chem With Implications for Air Quality, Journal of Geophysical Research:
802 Atmospheres, 124, 10109–10133, https://doi.org/10.1029/2019JD030248, 2019.

803 Pepin, N., Bradley, R. S., Diaz, H. F., Baraer, M., Caceres, E. B., Forsythe, N., Fowler, H., Greenwood, G., Hashmi,
804 M. Z., Liu, X. D., Miller, J. R., Ning, L., Ohmura, A., Palazzi, E., Rangwala, I., Schöner, W., Severskiy, I.,
805 Shahgedanova, M., Wang, M. B., Williamson, S. N., Yang, D. Q., and Mountain Research Initiative EDW Working

Group: Elevation-dependent warming in mountain regions of the world, Nature Climate Change, 5, 424–430, https://doi.org/10.1038/nclimate2563, 2015.

Pincus, R. and Baker, M. B.: Effect of precipitation on the albedo susceptibility of clouds in the marine boundary layer, Nature, 372, 250–252, https://doi.org/10.1038/372250a0, 1994.

Prein, A. F. and Heymsfield, A. J.: Increased melting level height impacts surface precipitation phase and intensity, Nature Climate Change, 10, 771–776, https://doi.org/10.1038/s41558-020-0825-x, 2020.

Prein, A. F., Langhans, W., Fosser, G., Ferrone, A., Ban, N., Goergen, K., Keller, M., Tölle, M., Gutjahr, O., Feser, F., Brisson, E., Kollet, S., Schmidli, J., Lipzig, N. P. M. van, and Leung, R.: A review on regional convection-permitting climate modeling: Demonstrations, prospects, and challenges, Reviews of Geophysics, 53, 323–361, https://doi.org/10.1002/2014RG000475, 2015.

Qian, Y., Yasunari, T. J., Doherty, S. J., Flanner, M. G., Lau, W. K. M., Ming, J., Wang, H., Wang, M., Warren, S. G., and Zhang, R.: Light-absorbing particles in snow and ice: Measurement and modeling of climatic and hydrological impact, Adv. Atmos. Sci., 32, 64–91, https://doi.org/10.1007/s00376-014-0010-0, 2015.

Ramanathan, V. and Carmichael, G.: Global and regional climate changes due to black carbon, Nature Geosci, 1, 221–227, https://doi.org/10.1038/ngeo156, 2008.

Ramanathan, V., Chung, C., Kim, D., Bettge, T., Buja, L., Kiehl, J. T., Washington, W. M., Fu, Q., Sikka, D. R., and Wild, M.: Atmospheric brown clouds: Impacts on South Asian climate and hydrological cycle, Proceedings of the National Academy of Sciences, 102, 5326–5333, https://doi.org/10.1073/pnas.0500656102, 2005.

Rangwala, I. and Miller, J. R.: Climate change in mountains: a review of elevation-dependent warming and its possible causes, Climatic Change, 114, 527–547, https://doi.org/10.1007/s10584-012-0419-3, 2012.

Rangwala, I., Miller, J. R., Russell, G. L., and Xu, M.: Using a global climate model to evaluate the influences of water vapor, snow cover and atmospheric aerosol on warming in the Tibetan Plateau during the twenty-first century, Clim Dyn, 34, 859–872, https://doi.org/10.1007/s00382-009-0564-1, 2010.

Rosenfeld, D.: TRMM observed first direct evidence of smoke from forest fires inhibiting rainfall, Geophysical Research Letters, 26, 3105–3108, https://doi.org/10.1029/1999GL006066, 1999.

Rosenfeld, D., Lohmann, U., Raga, G. B., O'Dowd, C. D., Kulmala, M., Fuzzi, S., Reissell, A., and Andreae, M. O.: Flood or Drought: How Do Aerosols Affect Precipitation?, Science, 321, 1309–1313, https://doi.org/10.1126/science.1160606, 2008.

Sadavarte, P., Rupakheti, M., Bhave, P., Shakya, K., and Lawrence, M.: Nepal emission inventory – Part I: Technologies and combustion sources (NEEMI-Tech) for 2001–2016, Atmospheric Chemistry and Physics, 19, 12953–12973, https://doi.org/10.5194/acp-19-12953-2019, 2019.

Saikawa, E., Panday, A., Kang, S., Gautam, R., Zusman, E., Cong, Z., Somanathan, E., and Adhikary, B.: Air Pollution in the Hindu Kush Himalaya, in: The Hindu Kush Himalaya Assessment: Mountains, Climate Change, Sustainability and People, edited by: Wester, P., Mishra, A., Mukherji, A., and Shrestha, A. B., Springer International Publishing, Cham, 339–387, https://doi.org/10.1007/978-3-319-92288-1_10, 2019.

Sarangi, C., Tripathi, S. N., Tripathi, S., and Barth, M. C.: Aerosol-cloud associations over Gangetic Basin during a typical monsoon depression event using WRF-Chem simulation, Journal of Geophysical Research: Atmospheres, 120, 10,974-10,995, https://doi.org/10.1002/2015JD023634, 2015.

Sarangi, C., Qian, Y., Rittger, K., Bormann, K. J., Liu, Y., Wang, H., Wan, H., Lin, G., and Painter, T. H.: Impact of light-absorbing particles on snow albedo darkening and associated radiative forcing over high-mountain Asia: high-

846 resolution WRF-Chem modeling and new satellite observations, Atmospheric Chemistry and Physics, 19, 7105–
847 7128, https://doi.org/10.5194/acp-19-7105-2019, 2019.

848 Shao, T., Liu, Y., Wang, R., Zhu, Q., Tan, Z., and Luo, R.: Role of anthropogenic aerosols in affecting different-
849 grade precipitation over eastern China: A case study, Science of The Total Environment, 807, 150886,
850 https://doi.org/10.1016/j.scitotenv.2021.150886, 2022.

851 Sharma, S., Chen, Y., Zhou, X., Yang, K., Li, X., Niu, X., Hu, X., and Khadka, N.: Evaluation of GPM-Era Satellite
852 Precipitation Products on the Southern Slopes of the Central Himalayas Against Rain Gauge Data, Remote Sensing,
853 12, 1836, https://doi.org/10.3390/rs12111836, 2020a.

854 Sharma, S., Khadka, N., Hamal, K., Shrestha, D., Talchabhadel, R., and Chen, Y.: How Accurately Can Satellite
855 Products (TMPA and IMERG) Detect Precipitation Patterns, Extremities, and Drought Across the Nepalese
856 Himalaya?, Earth and Space Science, 7, e2020EA001315, https://doi.org/10.1029/2020EA001315, 2020b.

857 Shige, S. and Kummerow, C. D.: Precipitation-Top Heights of Heavy Orographic Rainfall in the Asian Monsoon
858 Region, Journal of the Atmospheric Sciences, 73, 3009–3024, https://doi.org/10.1175/JAS-D-15-0271.1, 2016.

859 Sicard, P., Crippa, P., De Marco, A., Castruccio, S., Giani, P., Cuesta, J., Paoletti, E., Feng, Z., and Anav, A.: High
860 spatial resolution WRF-Chem model over Asia: Physics and chemistry evaluation, Atmospheric Environment, 244,
861 118004, https://doi.org/10.1016/j.atmosenv.2020.118004, 2021.

862 Sijikumar, S., Aneesh, S., and Rajeev, K.: Multi-year model simulations of mineral dust distribution and transport
863 over the Indian subcontinent during summer monsoon seasons, Meteorol Atmos Phys, 128, 453–464,
864 https://doi.org/10.1007/s00703-015-0422-0, 2016.

865 Soni, P., Tripathi, S. N., and Srivastava, R.: Radiative effects of black carbon aerosols on Indian monsoon: a study
866 using WRF-Chem model, Theor Appl Climatol, 132, 115–134, https://doi.org/10.1007/s00704-017-2057-1, 2018.

867 Talchabhadel, R., Karki, R., and Parajuli, B.: Intercomparison of precipitation measured between automatic and
868 manual precipitation gauge in Nepal, Measurement, 106, 264–273,
869 https://doi.org/10.1016/j.measurement.2016.06.047, 2017.

870 Terao, T., Islam, Md. N., Hayashi, T., and Oka, T.: Nocturnal jet and its effects on early morning rainfall peak over
871 northeastern Bangladesh during the summer monsoon season, Geophysical Research Letters, 33,
872 https://doi.org/10.1029/2006GL026156, 2006.

873 Tewari, M., Chen, F., Wang, W., Dudhia, J., LeMone, M. A., Mitchell, K., Ek, M., Gayno, G., Wegiel, J., and
874 Cuenca, R. H.: Implementation and verification of the unified NOAH land surface model in the WRF model, in:
875 20th conference on weather analysis and forecasting/16th conference on numerical weather prediction, 2165–2170,
876 2004.

877 Twomey, S.: The Influence of Pollution on the Shortwave Albedo of Clouds, J. Atmos. Sci., 34, 1149–1152,
878 https://doi.org/10.1175/1520-0469(1977)034<1149:TIOPOT>2.0.CO;2, 1977.

879 Vernier, J.-P., Thomason, L. W., and Kar, J.: CALIPSO detection of an Asian tropopause aerosol layer, Geophysical
880 Research Letters, 38, https://doi.org/10.1029/2010GL046614, 2011.

881 Wang, S., Zhang, M., Pepin, N. C., Li, Z., Sun, M., Huang, X., and Wang, Q.: Recent changes in freezing level
882 heights in High Asia and their impact on glacier changes, Journal of Geophysical Research: Atmospheres, 119,
883 1753–1765, https://doi.org/10.1002/2013JD020490, 2014.

884 Wu, L., Su, H., and Jiang, J. H.: Regional simulation of aerosol impacts on precipitation during the East Asian
885 summer monsoon, Journal of Geophysical Research: Atmospheres, 118, 6454–6467,
886 https://doi.org/10.1002/jgrd.50527, 2013.

887 Wu, L., Gu, Y., Jiang, J. H., Su, H., Yu, N., Zhao, C., Qian, Y., Zhao, B., Liou, K.-N., and Choi, Y.-S.: Impacts of
888 aerosols on seasonal precipitation and snowpack in California based on convection-permitting WRF-Chem
889 simulations, Atmospheric Chemistry and Physics, 18, https://doi.org/10.5194/acp-18-5529-2018, 2018.

890 Yang, Q., W. I. Gustafson Jr., Fast, J. D., Wang, H., Easter, R. C., Morrison, H., Lee, Y.-N., Chapman, E. G., Spak,
891 S. N., and Mena-Carrasco, M. A.: Assessing regional scale predictions of aerosols, marine stratocumulus, and their
892 interactions during VOCALS-REx using WRF-Chem, Atmos. Chem. Phys., 11, 11951–11975,
893 https://doi.org/10.5194/acp-11-11951-2011, 2011.

894 Zaveri, R. A. and Peters, L. K.: A new lumped structure photochemical mechanism for large-scale applications,
895 Journal of Geophysical Research: Atmospheres, 104, 30387–30415, https://doi.org/10.1029/1999JD900876, 1999.

896 Zaveri, R. A., Easter, R. C., Fast, J. D., and Peters, L. K.: Model for Simulating Aerosol Interactions and Chemistry
897 (MOSAIC), Journal of Geophysical Research: Atmospheres, 113, https://doi.org/10.1029/2007JD008782, 2008.

898 Zhang, Y. and Guo, Y.: Variability of atmospheric freezing-level height and its impact on the cryosphere in China,
899 Annals of Glaciology, 52, 81–88, https://doi.org/10.3189/172756411797252095, 2011.

900 Zhang, Y., Fan, J., Li, Z., and Rosenfeld, D.: Impacts of cloud microphysics parameterizations on simulated
901 aerosol–cloud interactions for deep convective clouds over Houston, Atmospheric Chemistry and Physics, 21, 2363–
902 2381, https://doi.org/10.5194/acp-21-2363-2021, 2021.

903 Zhao, C., Chen, S., Leung, L. R., Qian, Y., Kok, J. F., Zaveri, R. A., and Huang, J.: Uncertainty in modeling dust
904 mass balance and radiative forcing from size parameterization, Atmospheric Chemistry and Physics, 13, 10733–
905 10753, https://doi.org/10.5194/acp-13-10733-2013, 2013.

906 Zhao, C., Hu, Z., Qian, Y., Ruby Leung, L., Huang, J., Huang, M., Jin, J., Flanner, M. G., Zhang, R., Wang, H.,
907 Yan, H., Lu, Z., and Streets, D. G.: Simulating black carbon and dust and their radiative forcing in seasonal snow: a
908 case study over North China with field campaign measurements, Atmospheric Chemistry and Physics, 14, 11475–
909 11491, https://doi.org/10.5194/acp-14-11475-2014, 2014.

910

911

912   **Table 1** Model configuration.

Physics option	Scheme
Microphysics	Morrsion-2 moment (Morrison et al., 2009)
Radiation	Rapid Radiative Transfer Model for General Circulation Models (RRTMG; Iacono et al., 2008)
Land surface	Unified Noah (Tewari et al., 2004)
Planetary Boundary layer	Yonsei University (YSU; Hong et al., 2006)
Cumulus	Grell-3D for 9 km (Grell and Dévényi, 2002) and turned off for 3 km grid size nested domain.
Chemical and Aerosol mechanism	CBM-Z and MOSAIC 4-bin
Boundary Condition	ERA5 (meteorology) and CAM-Chem (Chemistry)

913

914

915
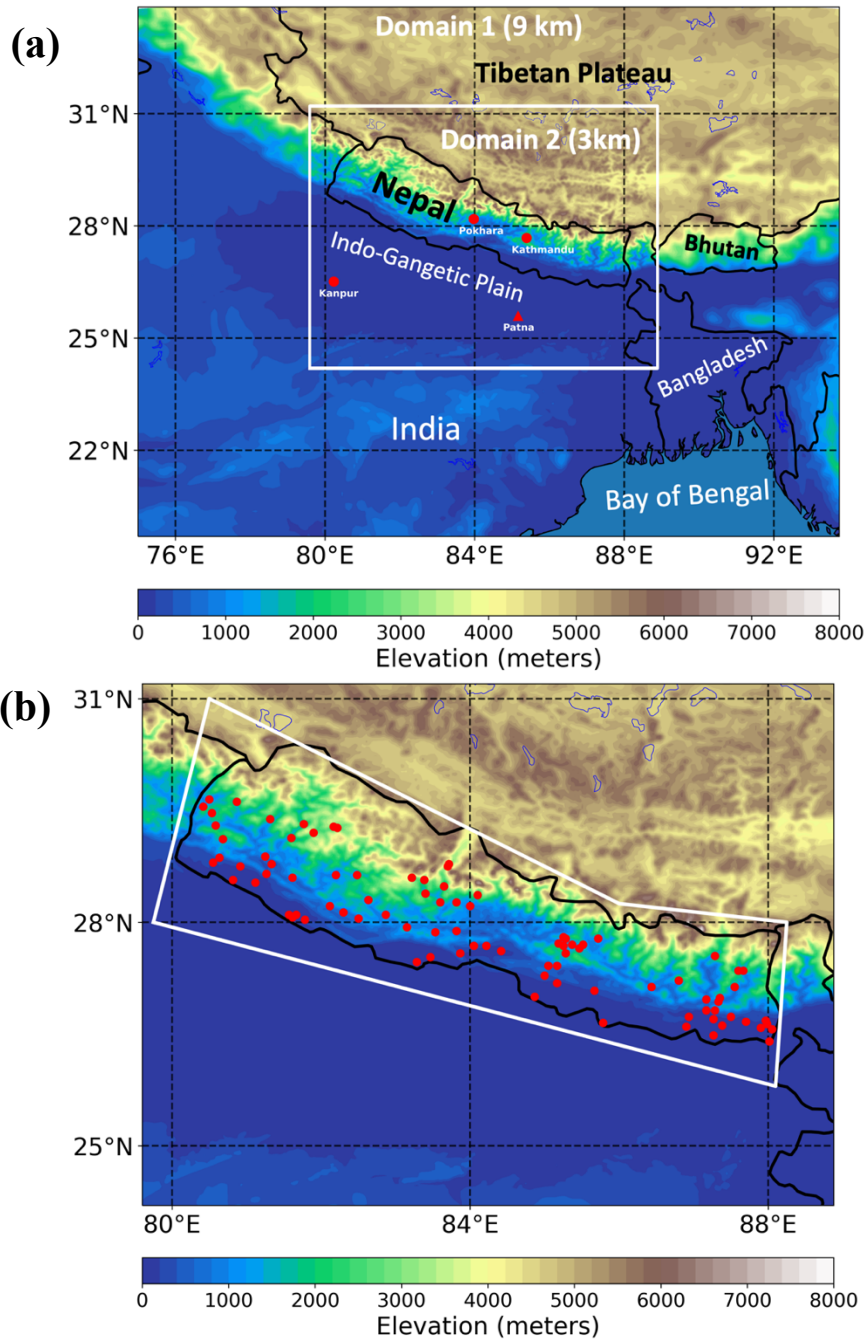
Figure 1 (a) The topography of the 9 km and 3 km nested grid size domains used in the simulation. The red marker represents the station locations for AERONET (circle) and upper air sounding (triangle). **(b)** The white-colored polygon represents the Central Himalayan region (CenHim) mentioned in the text. The red marker represents the locations of DHM Nepal rain gauge stations.

916
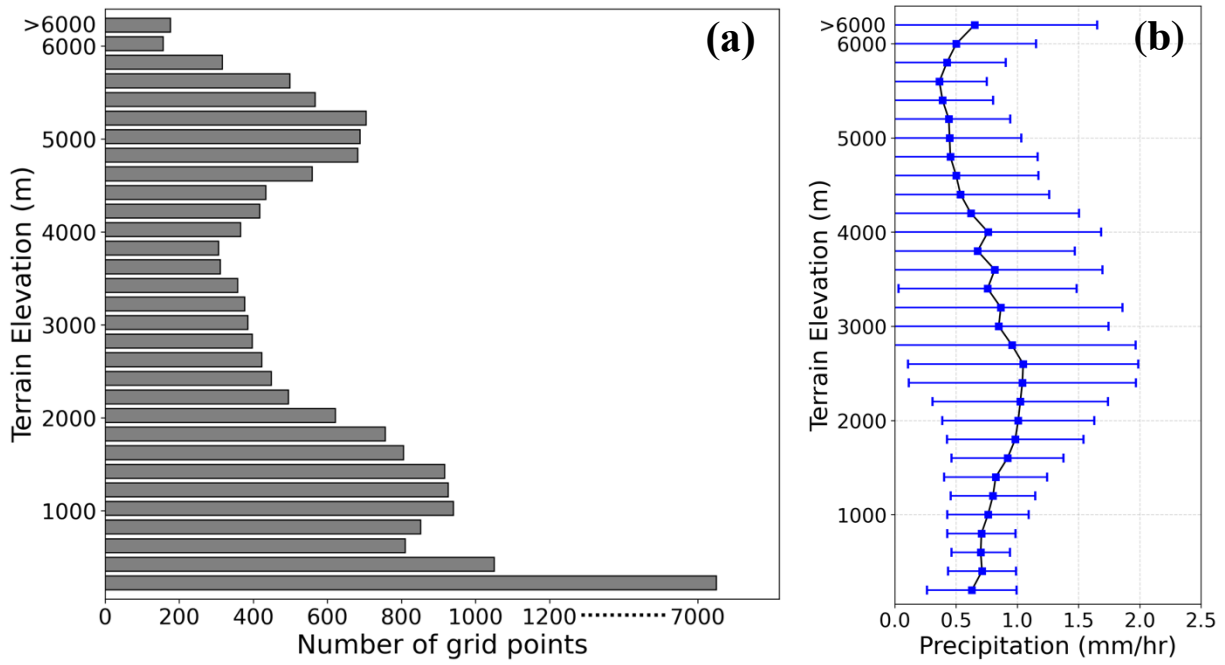
Figure 2 (a) The total number of grids per elevation range for 200 m bins up to 6000 m and one bin above 6000 m. **(b)** Variation of CTL mean (± 1 standard deviation) precipitation over the CenHim as a function of altitude.

917

918

919
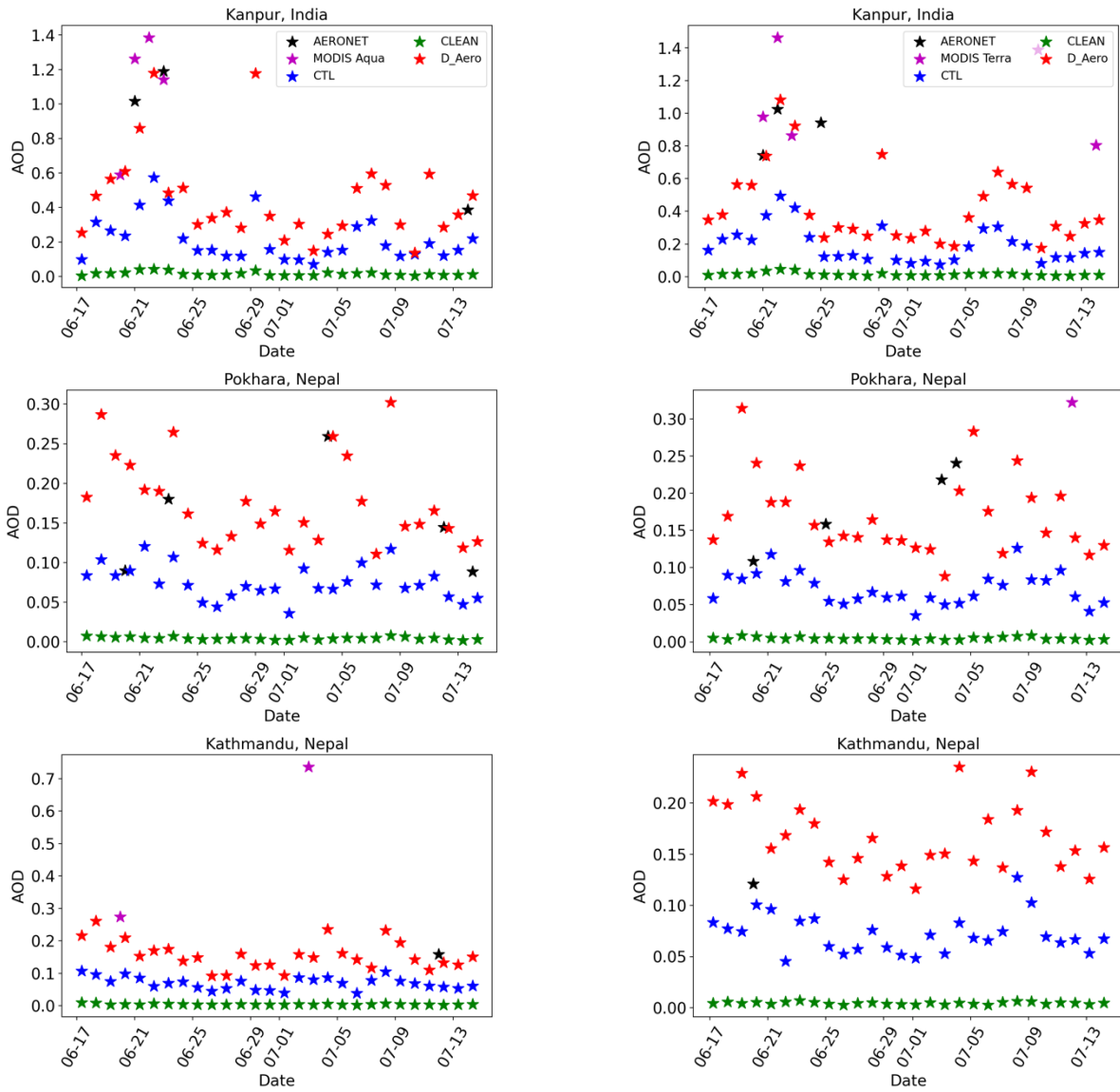
Figure 3 The simulated AERONET and MODIS Aqua (first column) and Terra (second column) AOD at three AERONET stations (Kanpur, Pokhara, and Kathmandu; see Fig. 1a for location).

920

921
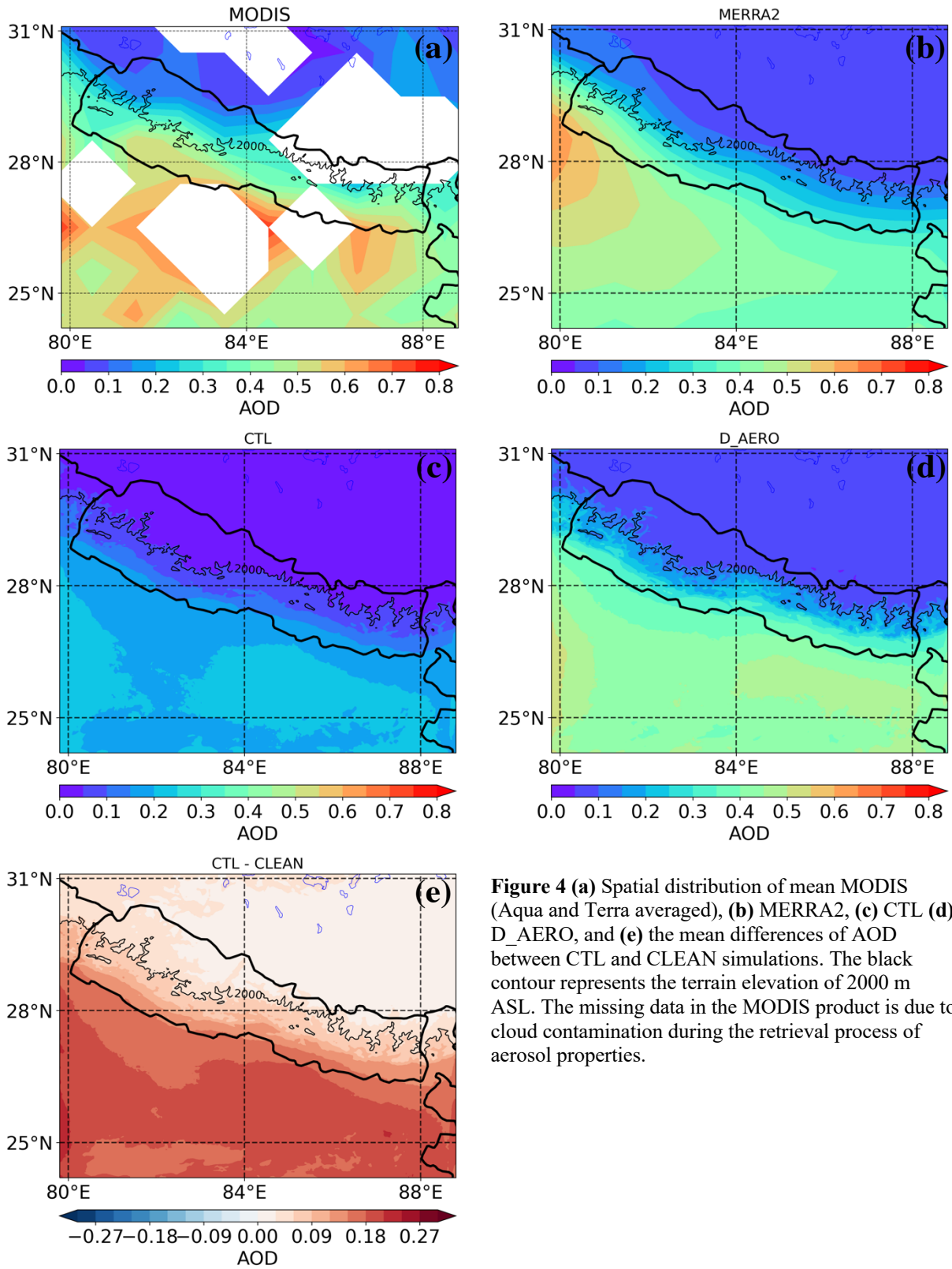
Figure 4 (a) Spatial distribution of mean MODIS (Aqua and Terra averaged), **(b)** MERRA2, **(c)** CTL **(d)** D_AERO, and **(e)** the mean differences of AOD between CTL and CLEAN simulations. The black contour represents the terrain elevation of 2000 m ASL. The missing data in the MODIS product is due to cloud contamination during the retrieval process of aerosol properties.

922
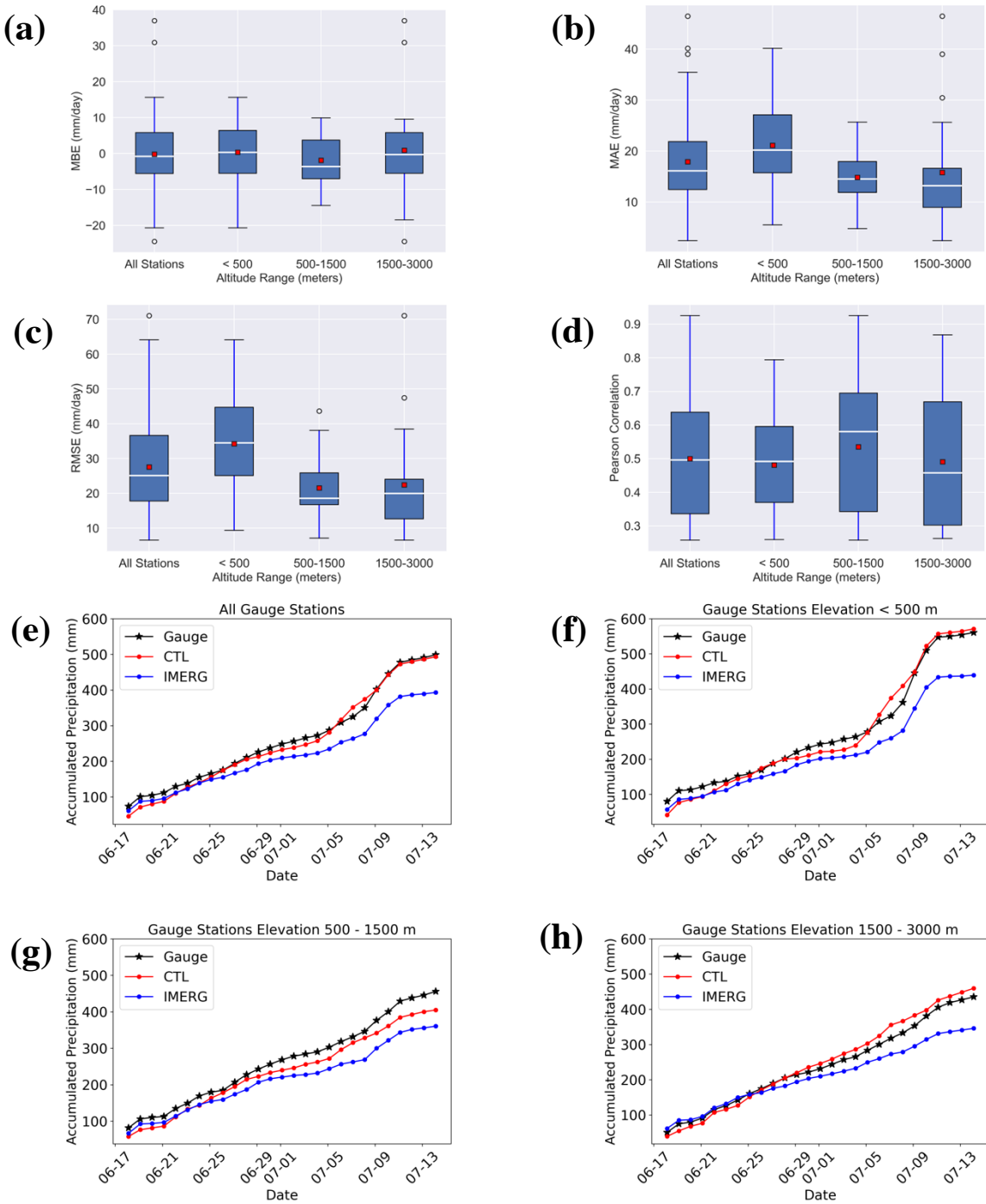
Figure 5 Box plots show the median, interquartile range, and extreme distribution for each of the error statistics [**(a)** MBE, **(b)** MAE, (**c**) RMSE, and **(d)** Pearson correlation] between the simulated and the rain gauge stations over Nepal, at an altitude that ranges below 500 m (41 stations), between 500 and 1500 m (28 stations), and between 1500 and 3000 m (21 stations). The red color marker at the center of the box represents the mean value. Time series of averaged accumulated precipitation at DHM rain gauge stations, CTL, and IMERG; **(e)** all rain gauge stations, stations located **(f)** below 500 m ASL, **(g)** between 500 and 1500 m, and **(h)** between 1500 and 3000 m terrain elevation.

923
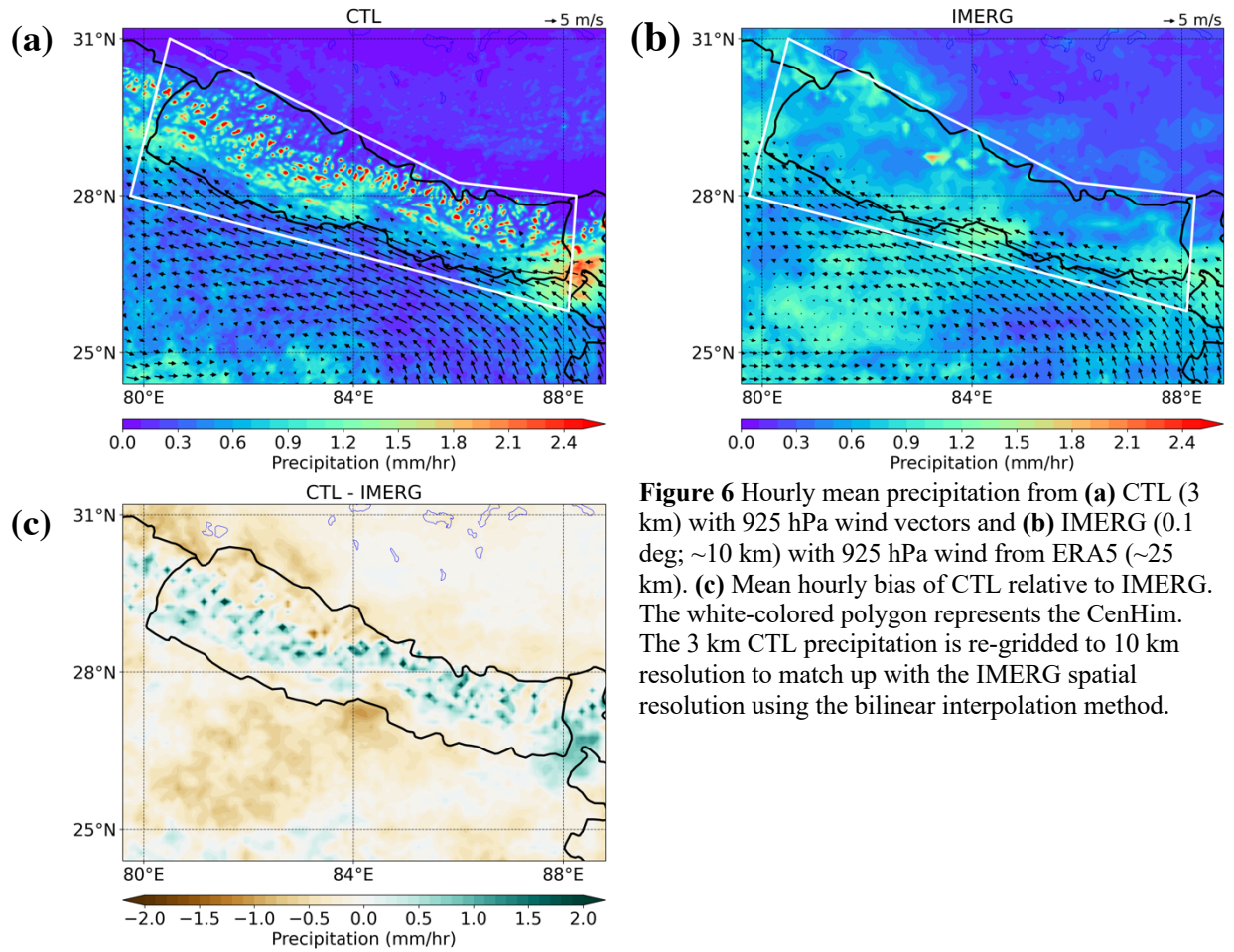
Figure 6 Hourly mean precipitation from **(a)** CTL (3 km) with 925 hPa wind vectors and **(b)** IMERG (0.1 deg; ~10 km) with 925 hPa wind from ERA5 (~25 km). **(c)** Mean hourly bias of CTL relative to IMERG. The white-colored polygon represents the CenHim. The 3 km CTL precipitation is re-gridded to 10 km resolution to match up with the IMERG spatial resolution using the bilinear interpolation method.

924

925

926
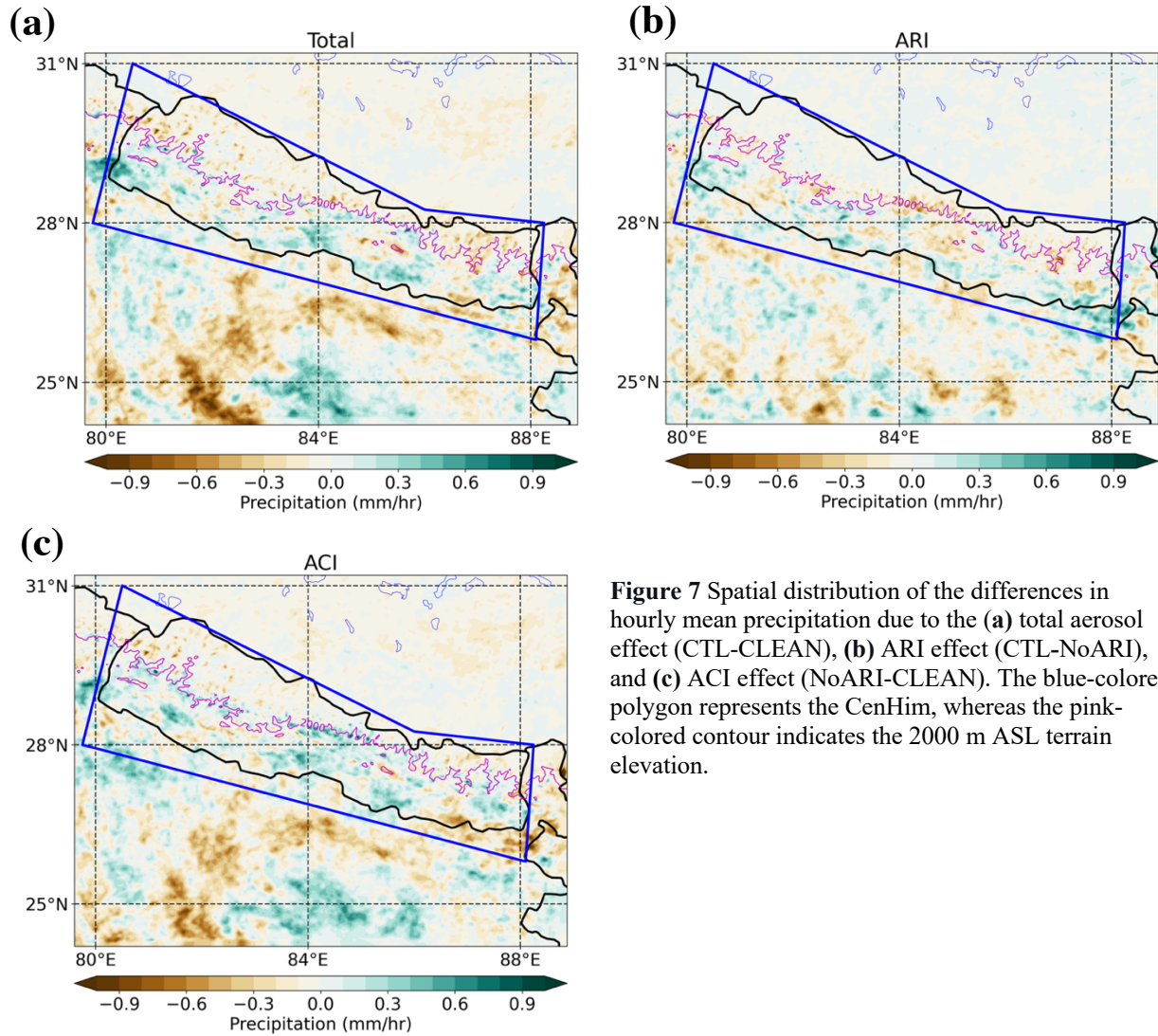
Figure 7 Spatial distribution of the differences in hourly mean precipitation due to the (a) total aerosol effect (CTL-CLEAN), (b) ARI effect (CTL-NoARI), and (c) ACI effect (NoARI-CLEAN). The blue-colored polygon represents the CenHim, whereas the pink-colored contour indicates the 2000 m ASL terrain elevation.

927

928
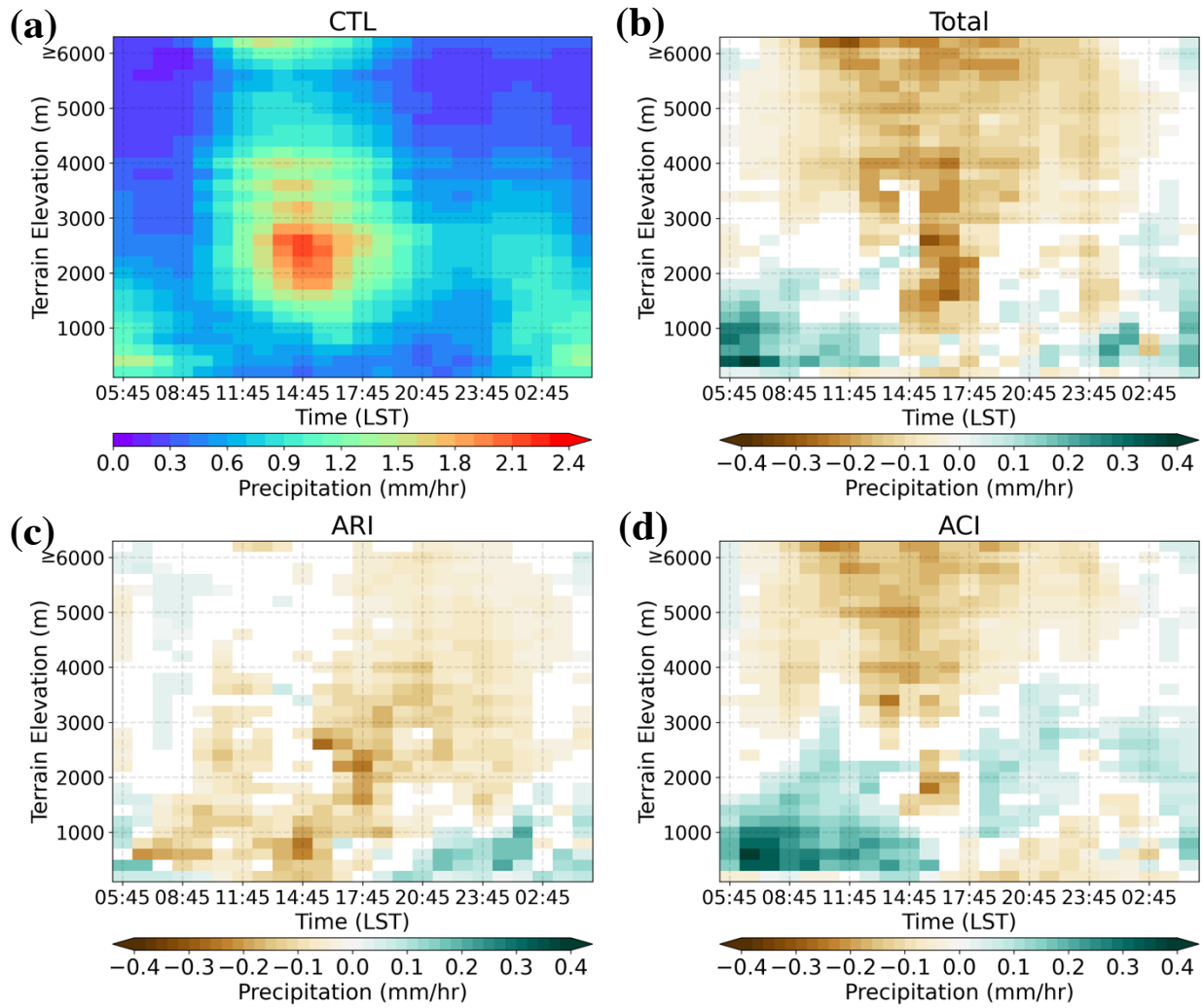
Figure 8 Diurnal-elevation **(a)** CTL precipitation, **(b)** aerosol effect (CTL-CLEAN), **(c)** ARI effect (CTL-NoARI), and **(d)** ACI effect (NoARI-CLEAN) and their diurnal variability. Only the differences that are significant at the 90 % confidence level based on the student t-test are plotted.

930

931
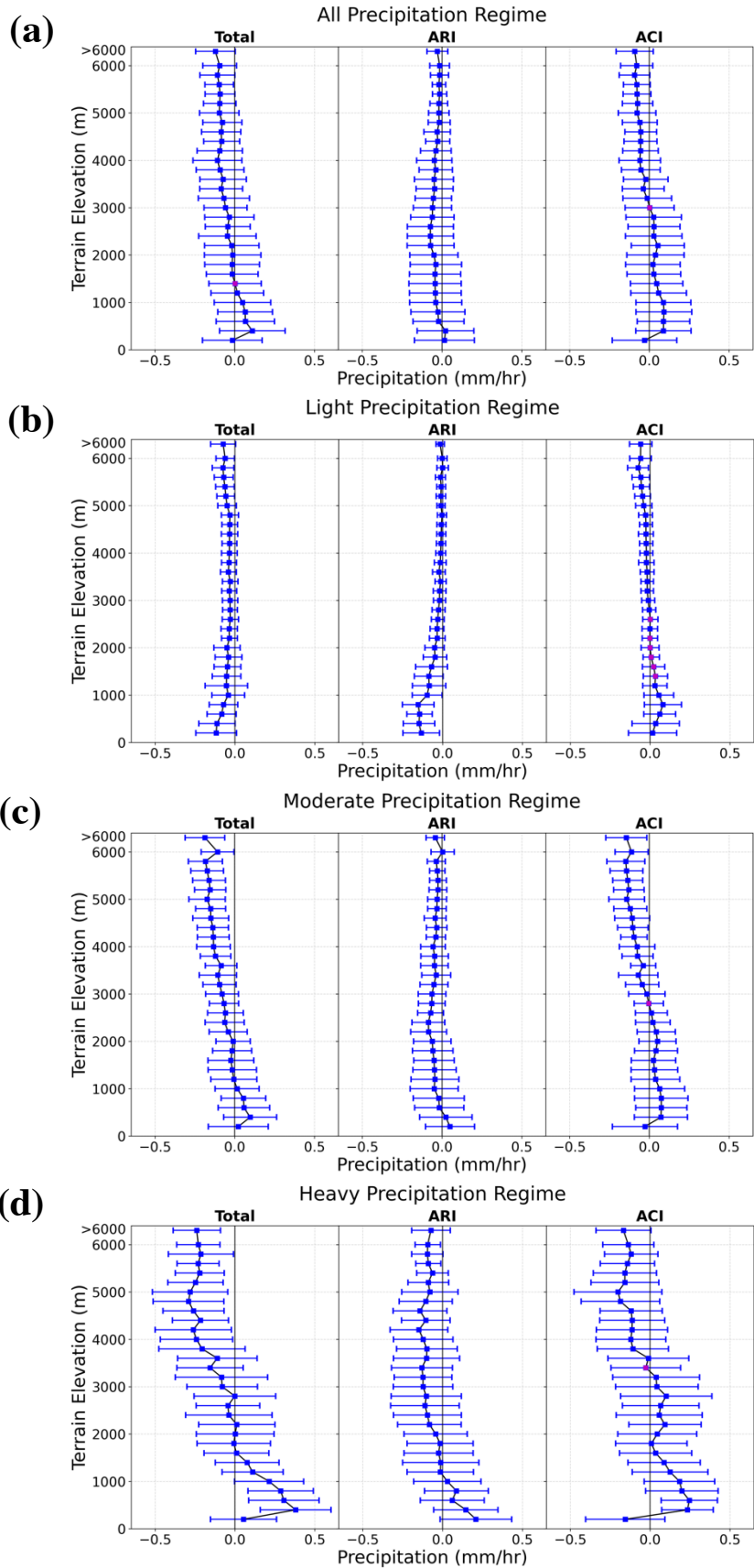
Figure 9 Elevational variability in different regimes [**(a)** all, **(b)** light, **(c)** moderate, and **(d)** heavy] precipitation differences due to aerosols. The blue dots and error bars represent the mean and ±1 standard deviation. The pink dot indicates that the differences between the two simulations are not significant at the 90% confidence interval based on the student t-test.

932

933

934
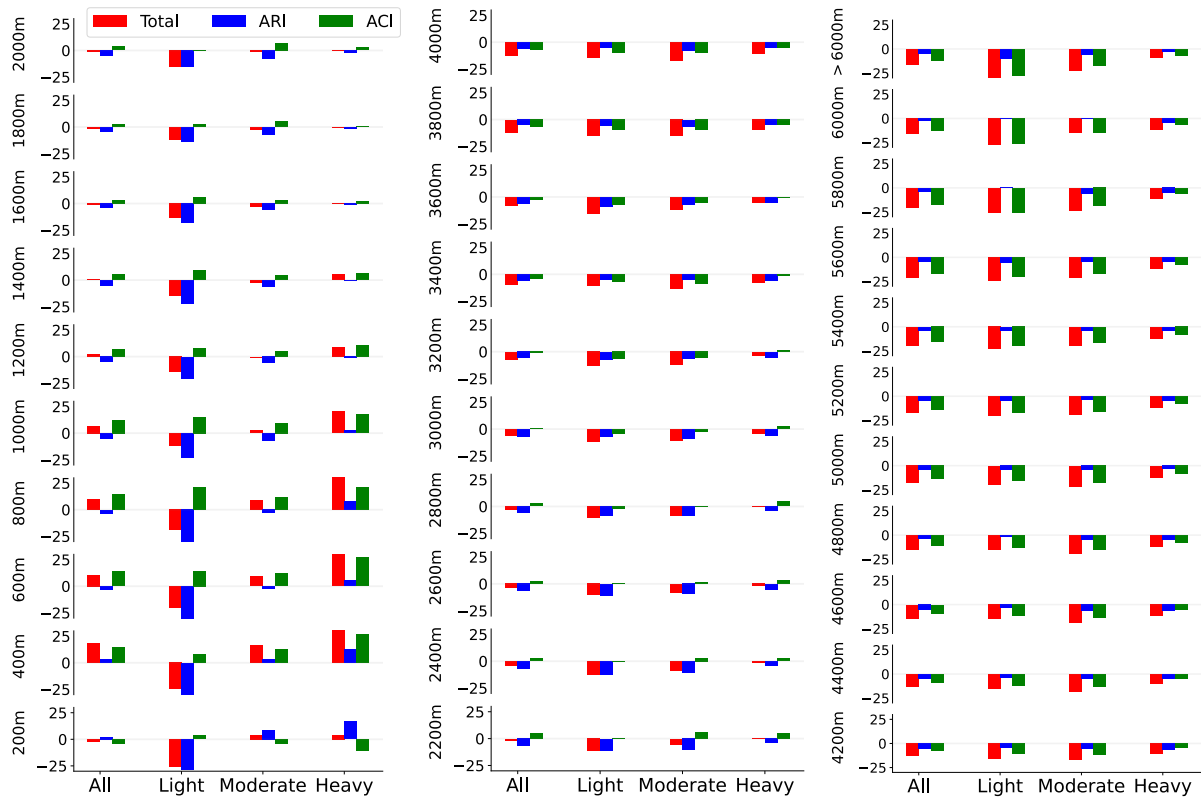
Figure 10 Relative change (%) in precipitation due to different effects of aerosols for all the elevational bins.

935

936

937
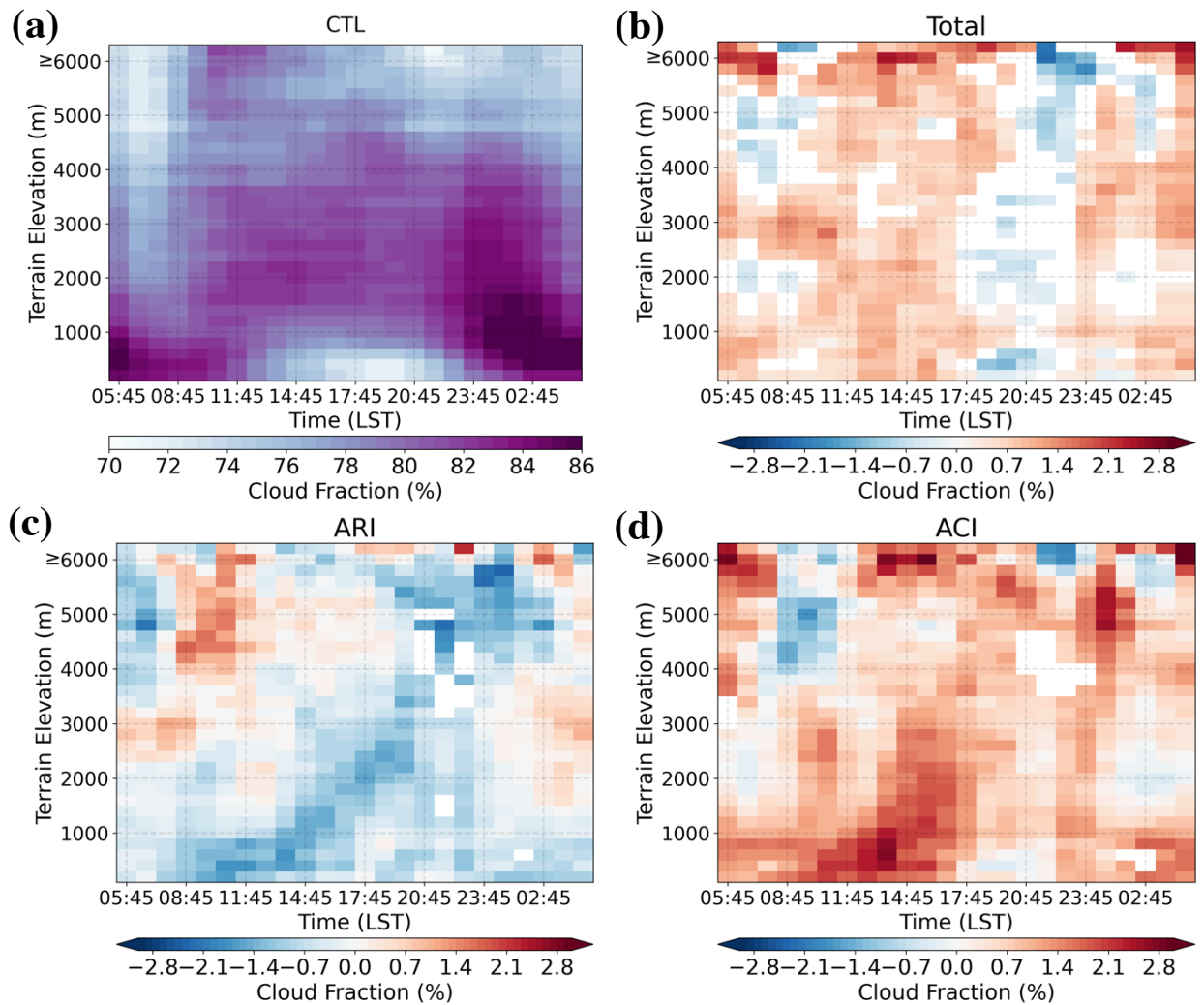
Figure 11 Diurnal-elevation of cloud fraction **(a)** CTL, and due to **(b)** aerosol effect (CTL-CLEAN), **(c)** ARI effect (CTL-NoARI), and **(d)** ACI effect (NoARI-CLEAN) and their diurnal variability. Only the differences that are significant at the 90 % confidence level based on the student t-test are plotted.

938

939
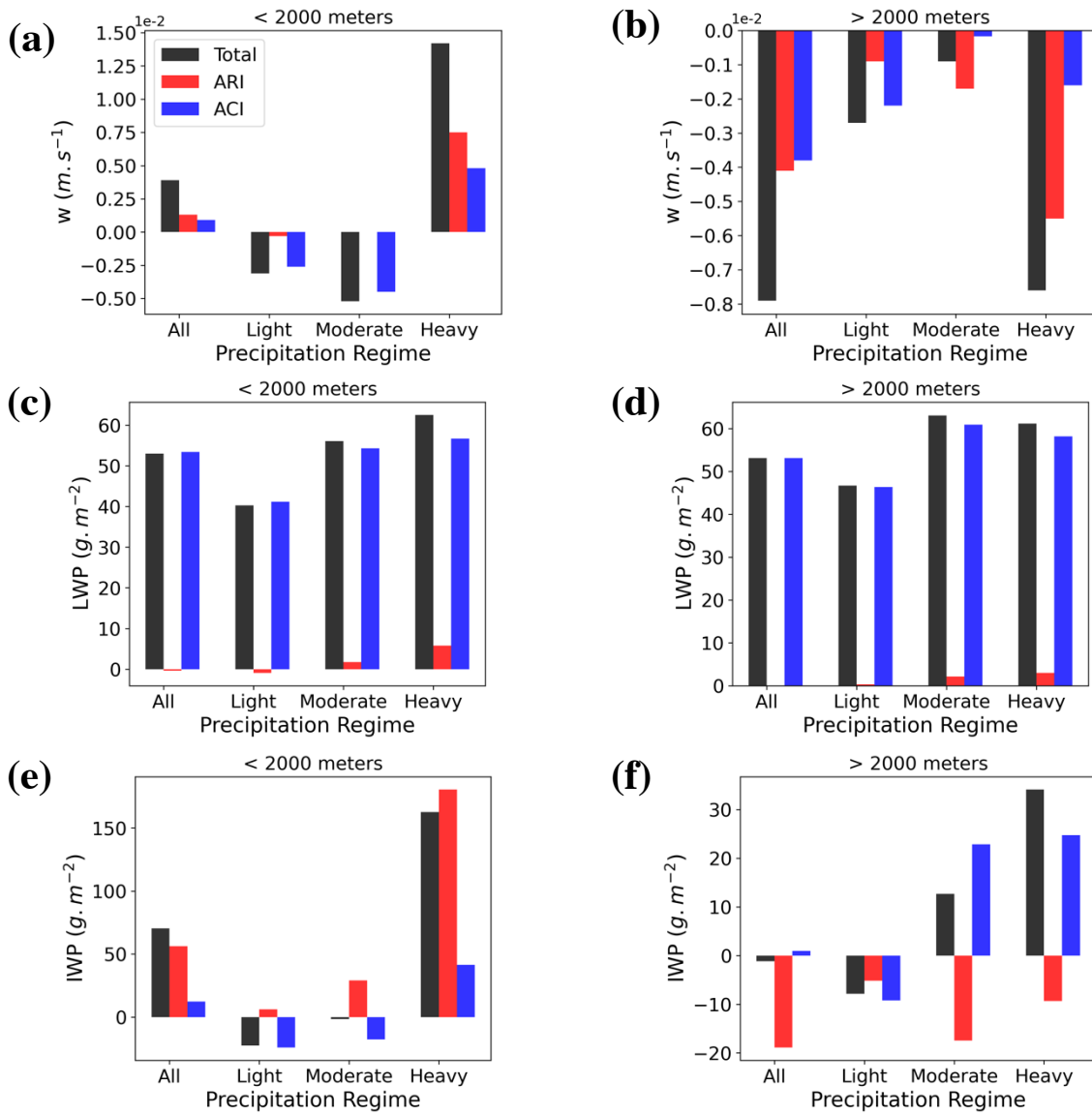
Figure 12 Mean perturbation of **(a, b)** vertical velocity, **(c, d)** LWP, and **(e, f)** IWP over the CenHim region for the terrain elevation below (first column) and above (second column) surface elevation of 2000 m ASL, for total, light, moderate, and heavy precipitation regime.

941

942
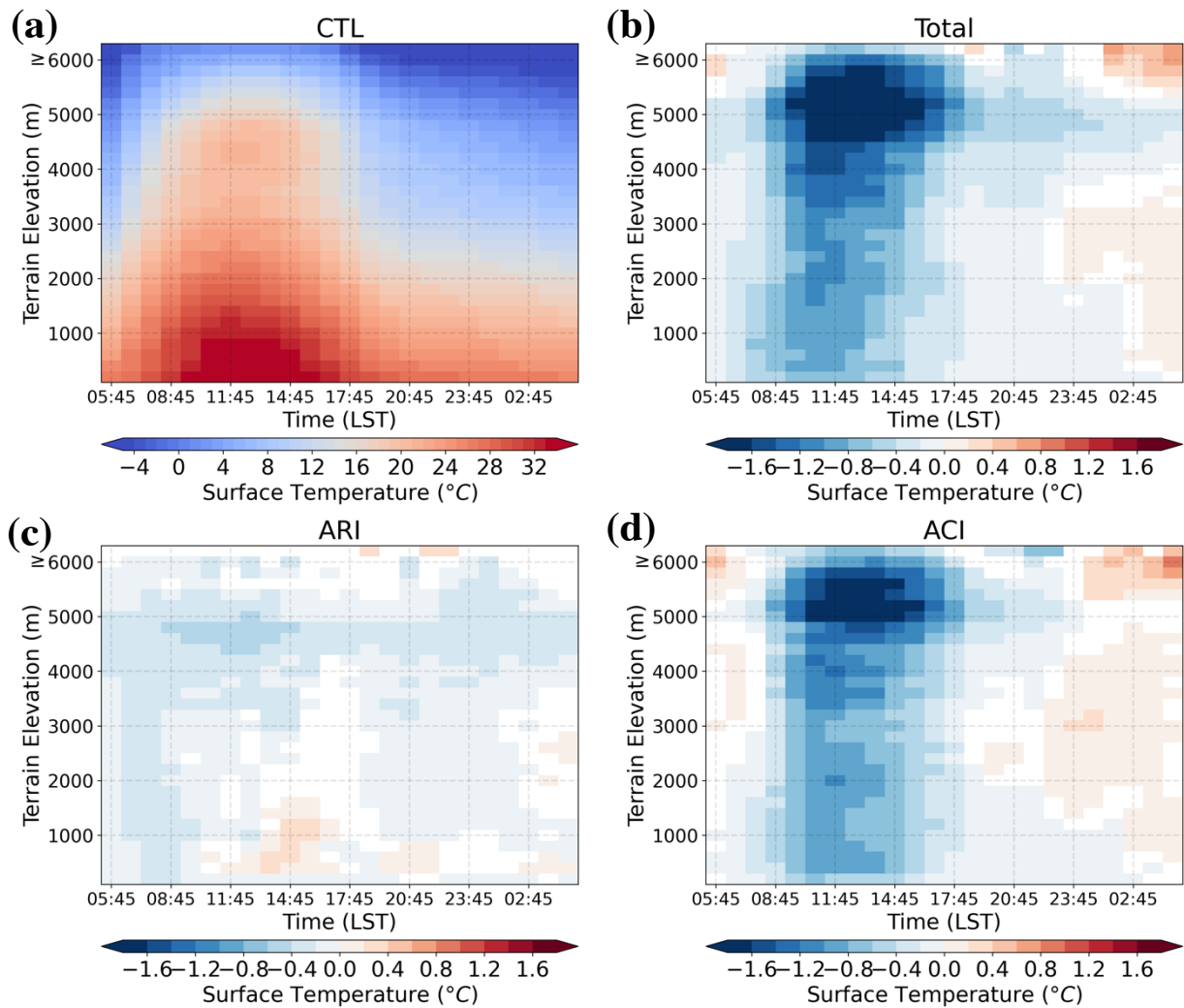
Figure 13 Diurnal-elevation of temperature **(a)** CTL simulated, and due to **(b)** aerosol effect (CTL-CLEAN), **(c)** ARI effect (CTL-NoARI), and **(d)** ACI effect (NoARI-CLEAN) and their diurnal variability. Only the differences that are significant at the 90 % confidence level based on the student t-test are plotted.
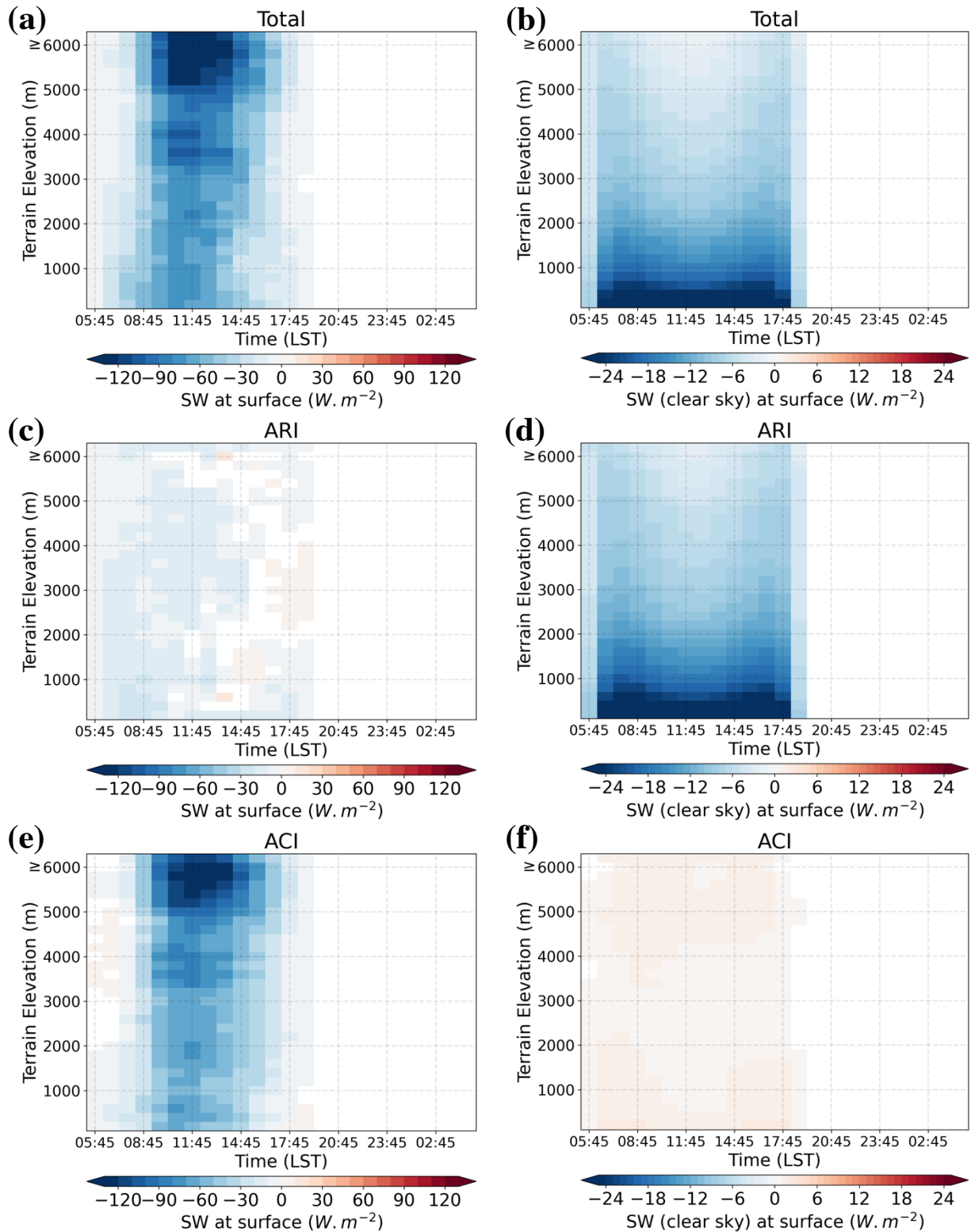
Figure 14 Diurnal-elevation all-sky (first column) and clear-sky (second column) downwelling shortwave radiation at the surface due to **(a, b)** aerosol effect (CTL-CLEAN), **(c, d)** ARI effect (CTL-NoARI), and **(e, f)** ACI effect (NoARI-CLEAN) and their diurnal variability. Only the differences that are significant at the 90 % confidence level based on the student t-test are plotted.

945

946
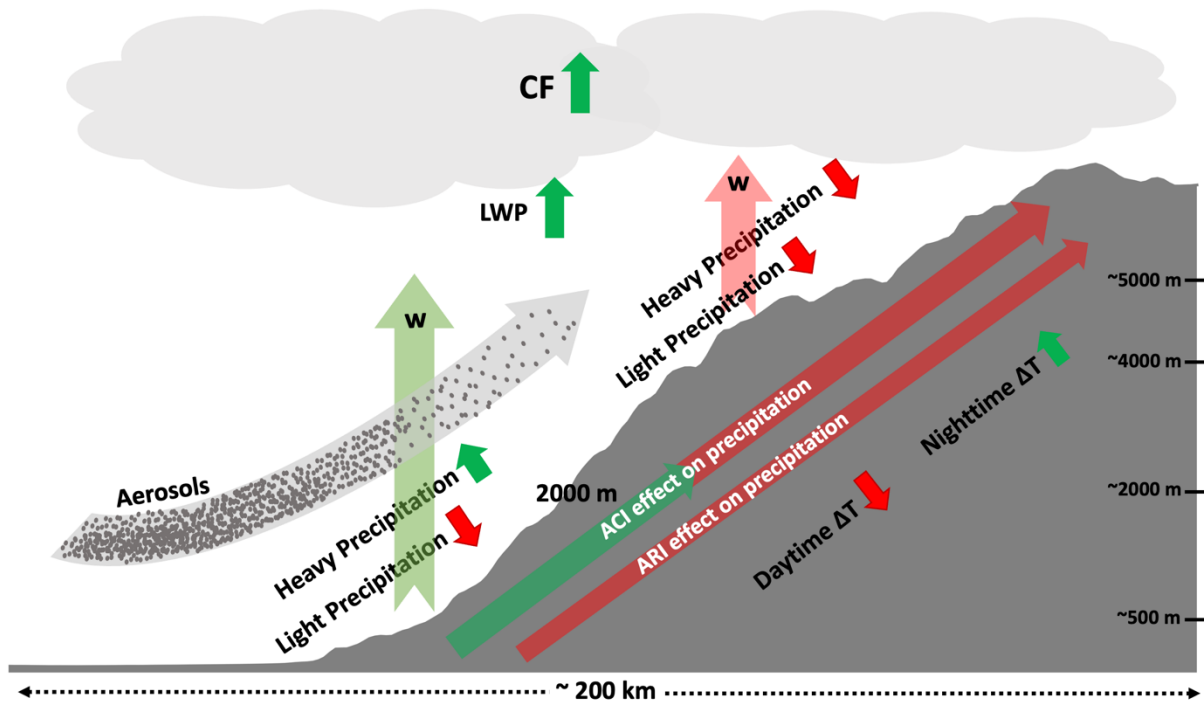
Figure 15 Schematic representing the relative impact of the different effects of aerosols on elevation-dependent precipitation. Green and red arrows represent the increasing and decreasing magnitude of different parameters, respectively. The shaded grey area represents the characteristic elevation of the southern slopes across the Central Himalayan region.

948